Directly irradiated liquid metal film in an ultra-high temperature solar cavity receiver. Part 1: Concepts and a quasi-steady-state analysis

Directly irradiated liquid metal film in an ultra-high temperature solar cavity receiver. Part 1: Concepts and a quasi-steady-state analysis

Tarek I. Abdelsalam[a,*], Zhao Tian[b], Adam Robinson[a]

[a] Institute for Energy Systems (IES), School of Engineering, The University of Edinburgh, Kings Buildings, Mayfield Rd, Edinburgh, EH9 3JL, United Kingdom.
[b] Centre for Energy Technology (CET), School of Electrical and Mechanical Engineering, The University of Adelaide, SA 5005, Australia.

Keywords: Analytical model; Solar thermal; High temperature; Liquid metal; Receiver; Efficiency

Abstract

Solar thermal energy has the theoretical potential to deliver heat at ultra-high temperatures (>1300 K), which can enable integration with state-of-the-art thermal energy storage systems and unlock new applications, including advanced power cycles and thermal processes. Liquid metals are prospective heat transfer fluids for such systems, given their favourable thermo-physical properties, while their aggressive corrosiveness is shown to be mitigated using compatible refractory containment materials. The conventional approach of collecting concentrated solar energy typically involves intermediate solid absorbers, in form of tubes or porous structures, which are prone to thermomechanical and chemical failure under high solar radiation. This paper investigates the use of directly irradiated liquid metal (tin) film, operating between 800-1673 K, in two possible cavity configurations: A 'reflective cavity' and an 'absorptive cavity'. The former employs cavity walls as internal reflectors to entrap radiation by secondary reflections until directly absorbed by the liquid metal. In the latter, the directly irradiated film is used to moderate the initial shot of concentrated solar radiation before diffusively reflecting them to the absorptive cavity walls, which perform as a radiative heat exchanger used to preheat the liquid metal. The concept performance is evaluated using an approximate quasi-steady-state energy model of the receiver. The reflective cavity performance is found strongly dependent on the optical properties of its internal surfaces, which resulted in poor efficiencies (<40%) without special treatments. The absorptive cavity demonstrated higher efficiencies (>70%) with greater insensitivity to the optical properties, hence, promoting its consideration in future developments of this concept.

Nomenclature

		Subscripts	
A	area (m^2)	a	ambient
I_{field}	average incident flux on field ($W.m^{-2}$)	abs	absorber(s)
CR	concentration ratio	ap	aperture
c_p	specific heat capacity ($J.kg^{-1}.K^{-1}$)	c	natural convection
E	Young's Modulus (Pa)	cav	cavity
F	view factor	e	emission
H	height (m)	$elec$	electrical
I	incident flux ($W.m^{-2}$)	in	input
h	convective heat transfer coefficient ($W.m^{-2}.K^{-1}$)	int	internal
		g	geometric

* Corresponding author. E-mail address: tarek.i.abdelsalam@ed.ac.uk.

k	thermal conductivity ($W.m^{-1}.K^{-1}$)	H	heliostats
L_{ch}	characteristic length (m)	o	optical
$\dot{m}$	mass flow rate ($kg.s^{-1}$)	r	radiation
Nu	Nusselt number	rec	receiver
P	power (W)	ref	reflection
$\dot{Q}$	rate of heat transfer (W)	rv	recovered
Ra	Rayleigh number	$abs, 2nd$	absorbed secondary reflections
T	temperature (K)	sol	solar
t	film thickness (m)	T	tower
v_{in}	inlet velocity ($m.s^{-1}$)	w	cavity walls
w	film width (m)	win	window
x	fraction of solar radiation missing the target surface		

Greek letters		*Abbreviations*	
ϵ	emissivity	CPC	compound parabolic concentrator
δ	thermal expansion coefficient (K^{-1})		
η	efficiency	CSP	concentrated solar power
λ	wavelength (μm)	HTF	heat transfer fluid
ρ	density ($kg.m^{-3}$)	LM	liquid metal
σ	Stefan-Boltzmann constant ($W.m^{-2}.K^{-4}$)	UHT	ultra-high temperature
σ_{th}	thermal stress (Pa)		
τ	transmissivity		
$\emptyset$	inclination angle (^{0})		
Ω	solid angle (sr)		

1. Introduction

Solar thermal energy can be used in various mechanical and thermochemical applications, including driving heat engines in Concentrated Solar Power (CSP) plants. In principle, the heat engine efficiency can be improved by increasing the hot source temperature; which is subjected to mechanical and material constraints (Çengel, 2019). Solar-only CSP systems are currently limited to temperatures <1000 K due to chemical limitations of molten salts used as the Heat Transfer Fluid (HTF) (Imran Khan et al., 2023). Running CSP at an Ultra-High Temperature (UHT) (>1300 K) would unlock the use of advanced power cycles, which can improve the solar-to-electricity efficiency by up to 50% (Kehlhofer et al., 2009; Stein and Buck, 2017). Alternatively, the sourced heat could be exploited in other UHT thermal applications, such as glass melting processes (Ahmad, 2017) or thermochemical water splitting for hydrogen production (Muhich et al., 2016). Thermal energy storage has been demonstrated viable at UHT, which promise high energy densities and roundtrip efficiencies (Amy et al., 2019; Datas, 2021; Robinson, 2017). Therefore, the missing link to a dispatchable UHT storage-integrated CSP is the provision of a UHT solar collector technology.

The proposed solution is investigated in three parts. This paper (Part 1) describes a novel UHT solar receiver based on a Liquid Metal (LM) HTF and investigates its performance using an analytical energy model. The transient fluid dynamics and radiation aspects of the concept will be addressed in Parts 2 and 3, respectively.

2. Central concepts for ultra-high temperature solar receivers

The fundamental conceptual elements of the proposed UHT solar receiver are outlined in this section, which serve as the base for the receiver design described in the next section.

2.1. Solar concentration

Given the ultra-high surface temperature of the Sun (5778 K), sustaining solar receivers at UHT is permitted by the second law of thermodynamics. Concentrating solar radiation is fundamental to sustaining an efficient radiative transfer at UHT (Ho and Iverson, 2014). Ideally, a concentration of 2050 suns is sufficient to maintain a spot at 2050 K (Fletcher, 2001); however, greater concentrations are required in practical applications to compensate for the incurred optical and thermal losses (Roldán Serrano, 2017; Steinfeld, 2002). While spillage losses may increase at higher concentrations, Li et al. (2019) found that the incorporation of a 3D compound parabolic concentrator (CPC) can minimise the spillage loss by >60%.

2.2. Cavity receiver

External receivers incur substantial thermal losses and are not recommended at temperatures >1000 K (Li et al., 2016). The UHT alternative is cavity receivers, which encloses and isolate the absorber from ambient effects. However, this benefit comes at the price of aperture-restricted contact with heliostats, and increased construction and O&M costs.

2.3. Liquid metal

LMs have been recommended in various studies as HTF in CSP systems (Frazer et al., 2014; Fritsch et al., 2015; Heinzel et al., 2017; Lorenzin and Abánades, 2016; Pacio and Wetzel, 2013; Pacio et al., 2013). The replacement of the conventional 'solar salts' (nitrates) with LMs was estimated to improve the receiver efficiency by 20% at 2000 suns and 1173 K (Pacio et al., 2013) and reduce the levelised cost of producing electricity by up to 15% (Singer et al., 2010). In addition to their high boiling points and thermal conductivities, LMs offer a single-phase heat transfer process over a wide range of temperatures (Table 1).

Heavy metals, such as tin, are characterised by their high boiling points and chemical stability at UHT. Their high volumetric heat capacities and densities also facilitate compact receiver designs. Their low specific heat capacities could be compensated by their wide liquid ranges. However, they are disadvantaged by their increased corrosiveness at UHT (Lorenzin and Abánades, 2016; Pacio and Wetzel, 2013). Zhang et al. (2018) confirmed that commercially available tubes made from graphite, silicon carbide and mullite could provide effective containment for molten tin at 1623 K. Tin is characterised by its low vapour pressure (0.0904 Pa) compared to other LMs at 1300 K, such aluminium (18.548 Pa), lead (129.81 Pa), and Bismuth (1002.9 Pa) (Hildebrand, 1918). Therefore, vaporisation losses from tin is projected to be substantially lower than other LMs. Molten tin was suggested by Zheng and Xu (2018) as HTF in a hypothetical solar tower system used for hydrogen production.

Pumping LMs at UHT can be a concern. While electromagnetic pumps might be favoured over mechanical pumps in terms of maintainability and durability at UHT, their efficiencies are significantly lower for pumping heavy metals (Fritsch et al., 2015). Continuous pumping of molten tin at 1673 K for 72h was demonstrated by Amy et al. (2017), which displayed minimal failure to the containment components.

Table 1
Thermo-physical properties of selected HTFs at high temperatures (Assael et al., 2006; Assael et al., 2010; Çengel, 2019; Leitner et al., 2017; Lorenzin and Abánades, 2016; Morita *et al.*, 2006; Romero and González-Aguilar, 2016; Sharafat and Ghoniem, 2000; Sobolev, 2010).

Fluid	Density ($kg.m^{-3}$)	Specific heat capacity ($J.kg^{-1}.K^{-1}$)	Liquid range (K)	Thermal conductivity ($W.m^{-1}.K^{-1}$)	Dynamic viscosity (mPa.s)
Aluminium (at 1600 K)	2192	1080	933-2743	237	~0.750
Tin (at 1236.5 K)	6526	255	505-2875	66.8	0.805
Lead-bismuth eutectic (at 1073 K)	9710	146	397-1943	17.7	1.33
Sodium (at 1100 K)	761	1260	371-1156	63.3	0.18
Solar salt (at 800 K)	<1500	1520	533-838	0.53	1.69
Air (at 1223 K)	0.289	1176	N/A	0.077	0.047

2.4. Direct irradiation

The absorption of concentrated solar radiation is conventionally handled by a solid absorber, which then transmits the heat to the HTF by convection and conduction. For a transparent HTF, air or water, an intermediate opaque absorber is required to absorb the radiation despite adding parasitic resistance to heat flow. Directly irradiated heat exchangers and tubular receivers cannot deliver outlet HTF temperature >1100 K due to the risk of developing thermal stresses, leading to material degradation, under high solar fluxes (Charpentier et al., 2012; Ho, 2016).

Particle receivers use directly illuminated ceramic particles as heat transfer and storage mediums at temperatures ≤1273 K (Diago et al., 2018; Ho, 2016; Wu et al., 2014). However, the solar-weighted absorptance of particles exposed to air for 24 hours was found to deteriorate when temperature increased from 973 K to 1273 K (Siegel et al., 2014). This cyclic decay has raised concerns over the durability of particle receivers at UHTs. Direct absorption by molten salts was also considered in designs of external and cavity receivers; however, performance was limited by wind-induced disruptions (Bohn, 1987; Ho and Iverson, 2014). Optically exposed mercury was suggested by Tammen and Bobby (1984) as an HTF and reflector in a dish receiver.

2.5. Direct absorption by the liquid metal

The low emissivity/absorptance of LMs might not prohibit them as solar absorbers. The influence of cavity emissivity on the receiver efficiency was found minimal (<5%) (DeAngelis et al., 2018; Fang and Wei, 2014). Additionally, LM emissivities increase with temperature, which may exceed 0.2 for molten tin at UHT (Greenstein, 1989; Jack et al., 1969). The solar absorptance can be furtherly enhanced by colouration or addition of absorptive ceramic particles (Hou et al., 2018; Phelan et al., 2013). The emissivities of different LMs are presented in Table 2.

Table 2
Spectral emissivities of different liquid metals. The emissivity values here are average values evaluated at the stated temperatures.

Liquid metal	Wavelength (nm)	Temperature (K)	Emissivity	Source
Aluminium	500	1173	0.070-0.100	(Kohl et al., 2022)
Copper	632.8	1000	0.040	(Krishnan and Nordine, 1993)
	514.5	1400	0.300	
Gold		1400	0.470	
Iron	630.0	2022	0.475	(Dubrovinsky and Saxena, 1999)
Nickel	514.5	1800	0.410	(Krishnan and Nordine, 1993)
Palladium		1950	0.380	
Platinum		2250	0.450	
Silver	632.8	1300	0.050	
Tin	532.0	1400	0.280	(Greenstein, 1989)
Zirconium	632.8	2125	0.350	(Krishnan and Nordine, 1993)

In view of the previous discussion, the proposed UHT receiver will feature direct absorption by molten tin in a cavity receiver operating under high solar concentration. In the following sections, description of the receiver design is presented, followed by an energy analysis.

3. Design description

The proposed receiver is designed for a hypothetical solar tower system with specifications presented in Table 3. The field is estimated to deliver 101.64 MW at 6750 suns to the receiver. This concentration level is equivalent to medium-power lasers used in etching semiconductor materials (Nath, 1988). Yet, this concentration level has not been demonstrated in commercial CSP, which are still limited to <1000 suns, mainly due to material constraints of conventional tubular receivers when operating at high solar fluxes (Imran Khan et al., 2023). Solar tower systems can deliver up to 5000 suns with a room for further concentration, theoretically up to 23,000 suns for a rim angle of 45^0 (Steinfeld and Palumbo, 2001), by incorporating non-imaging secondary concentrators, such as CPCs (Becker and Vant-Hull, 1991; Li et al., 2016; Schmitz et al., 2006; Welford and Winston, 1989). A 3D CPC was demonstrated by Li et al., (2019) to increase the flux concentration from a multi-source simulator by 4.1X at 3000 suns. The design, cooling, and manufacturing of the CPC are not covered in this paper; however, it is projected to be a metallic structure with a similar water-cooling system as described by Li et al. (2019). The prospect of using the cavity fluid CPC coolant is yet to be investigated. While this study covers only the receiver technology, future work may involve optimising the heliostats layout for the proposed receiver, which may benefit from Pitz-Paal (2011) and Segal (2012) in accounting for the constrained CPC acceptance.

Table 3
Energy and geometrical specifications of the hypothetical solar field used as input conditions to the receiver model.

Annual Solar Resource (kWh.m^{-2})	Total Aperture Area of Heliostats (m^2)	Geometrical Concentration Ratio	Overall Optical Efficiency
2012	150,600	10,000	67.5%

The proposed receiver here supplies heat to a circulating molten tin, as demonstrated in Fig. 1, to raise its temperature to 1673 K, which would enable integration with a CCGT cycle. The low temperature was set at 800 K based on an LM cycle in a literature UHT thermal energy storage (Robinson, 2017), which coincidentally provides a safe tolerance above the melting temperature of tin. Anti-freezing measures employed for LMs in nuclear and CSP plants (Deng et al., 2021; Frignani et al., 2019; Kotzé et al., 2011) can be utilised to prevent HTF solidification during the diurnal cycle.

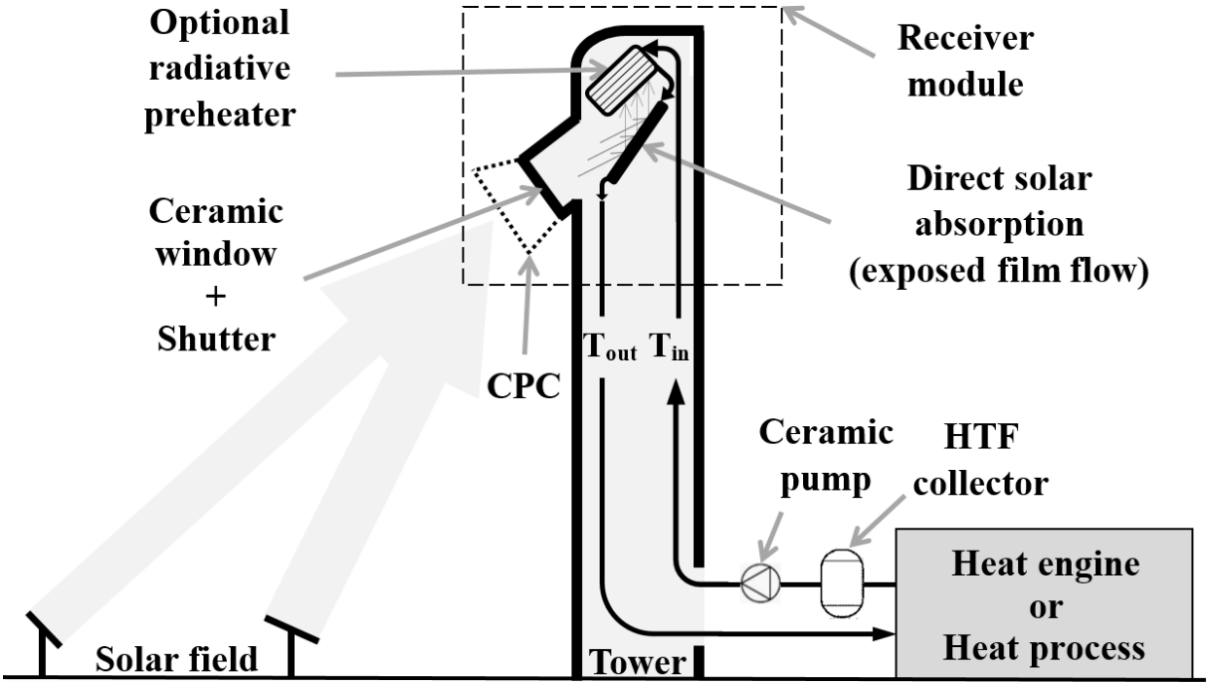

Fig. 1. A process diagram of the proposed receiver in a generic HTF circuit. T_{in} and T_{out} are the inlet and outlet temperatures of the HTF to and from the receiver module, respectively. The aperture window incorporates a shutter (mechanical or electrochromic) to minimise the radiative losses during non-operational periods.

The molten tin circuit can be constructed using mechanical and sealing components developed by Amy et al. (2017) and containment materials recommended by Zhang et al. (2018). Although the manufacturability of curved geometries with brittle ceramics could be challenging, it may become viable with the advancement of large-scale rapid prototyping and other fabrication techniques. Fabrication of curved and complex ceramic structures was demonstrated using additive manufacturing (Klosterman et al., 1999, Lakhdar et al., 2021; Mohammadi et al., 2022), which are currently being used in manufacturing graphite enclosures and components in marine and automotive applications (Graphite AM, 2022). The proposed receiver can also benefit from the existing base of practical experience with handling molten tin at UHT in the 'Pilkington' process, where an inert atmosphere of N_2 and H_2 is used to protect against oxidation (Francis, 2016; Pilkington, 1969). This measure would also protect the containment materials from oxidation and burning at UHT.

The proposed receiver module is displayed in Fig. 2. The cuboidal cavity shape was chosen, as it offers thermal (Lakshmipathy et al., 2020) and optical (Arrif et al., 2021) advantages over cylindrical cavities. The aperture plane is tilted 30^0 downward to compensate for the restricted CPC acceptance angle (Hoffschmidt et al., 2012; Vant-Hull, 2021). For un-windowed apertures, this tilting helps minimising the wind-induced convection and disruption of fluidic seals (Flesch et al., 2014). The aperture diameter was determined based on the required flux following the guidance from Steinfeld and Schubnell (1993).

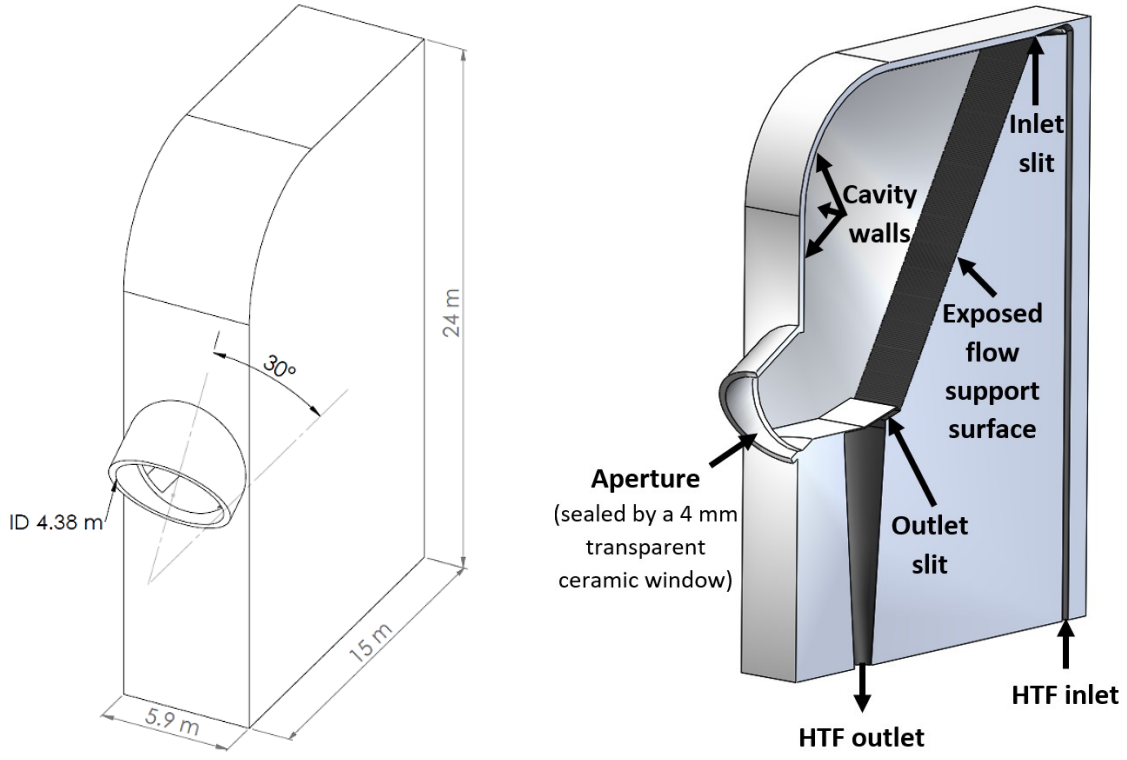

(a) (b)

Fig. 2. Illustrative sketches of the receiver module displaying (a) the external dimensions of the module at the studied scale and (b) labelled sectional view of the receiver (the optional tubular preheater at cavity walls is not included in this figure). The wall thickness is 0.55 m.

3.1. Inclined film flow

A 'free-fall' flow configuration was initially considered to minimise the receiver size. This configuration is employed in particle receivers and was found inefficient due to the uncontrolled gravitational acceleration, which minimalises the residence time required for heat transfer (Ho et al., 2019). This limitation is likely more severe in the cases of dense and less absorptive LM. Consequently, the HTF here is inserted as a film flowing over an inclined surface to reduce the gravitational component and enable control over the flow. Flow inclination reduces the view factor with the aperture; hence, minimises the re-radiated losses from the film. However, increasing the inclination angle (Ø) expands the cavity depth, and would require heliostats relocation farther away from the tower, as illustrated in Fig. 3, resulting in reduced land utilisation and increased spillage. Therefore, a supplementary hydrodynamic control measure is necessary to maintain the film continuity at a reasonable flow inclination (Ø=30^0). In Part 2, surface corrugations are demonstrated effective in preserving the film continuity.

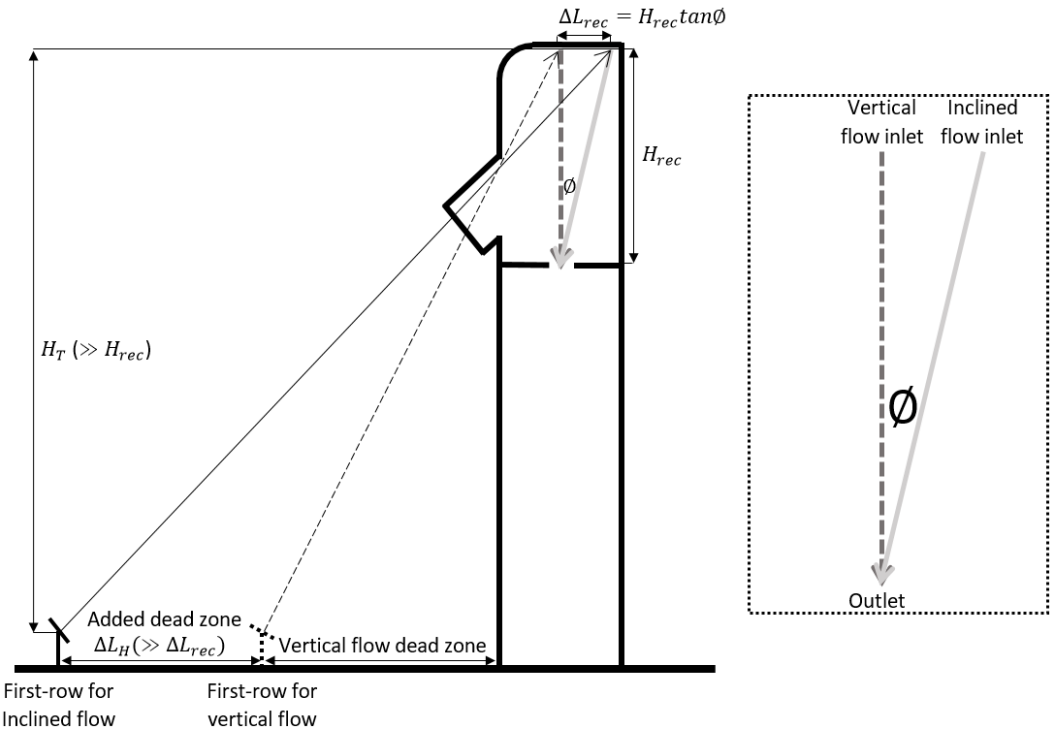

Fig. 3. A simplified beam diagram showing the adverse implications of inclining the HTF flow relative to a vertical flow. To compensate for the reduced projected HTF area, which would shrink by a factor of cos∅, the depth of the receiver will need to expand by ΔL_{rec}, while the first row of heliostats will need to be displaced at a much farther distance (ΔL_H), as it is a function of the tower height (H_T). H_{rec} is the receiver height. The dashed arrows represent the vertical flow configuration, while the solid arrows represent the inclined flow configuration.

3.2. Transparent ceramic window

For receivers enclosing directly irradiated fluids/particles, it is recommended to seal the aperture with transparent windows to prevent leakage and oxidation (Romero and González-Aguilar, 2016). While fluidic seals can be an optically efficient alternative to glazed windows, their contemporary technologies are still underdeveloped to effectively seal the aperture against oxygen diffusion and transient wind conditions (Alipourtarzanagh et al., 2020; Tan et al., 2009). Windows can have the advantage of being spectrally selective to facilitate a "one-way" passage for solar radiation by maximising transmittance at the peak solar wavelength and maximising reflectance across the infrared range where blackbody emissions peak at the cavity temperature (Maag et al., 2011; Romero and Steinfeld, 2012). Concerns over window cleaning can be mitigated through the ongoing development of transparent anti-soiling coatings for solar applications (Dahlioui et al., 2022, Huang et al., 2021, Ilse et al., 2019, Quan and Zhang, 2017, Zhang et al., 2019), which were proven feasible for solar thermal systems (Lorenz et al., 2014). Windows exposed to UHT liquid metals in closed environments may be subjected to the corrosive and opaque metallic vapours, which may be alleviated by running fluidic curtains on their interior surfaces.

Glass windows are often made thicker than optically desired to withstand the thermal stresses at UHT (Ambrosetti and Good, 2019; Becker et al., 2014). For a pressurised cavity receiver at 1973 K under 10,000 suns, a quartz glass window thickness of 10-20 mm was required (Karni et al., 1998). Glass windows are limited to diameters <1 m (Ávila-Marín, 2011; Hinkley et al., 2019; Romero and González-Aguilar, 2014) and not recommended for temperatures >1073 K (Röger et al., 2006). Transparent ceramics offer a promising glazing alternative, which avoids the structural limitations of quartz glass at UHT, with prospective large-scale manufacturability (Goldman et al., 2017; Sepulveda et al., 2013), which promoted them in solar thermal (Erickson and Gavilan, 2016) and photovoltaic

(Liu et al., 2011) applications. Magnesium-aluminate-spinel ($MgAl_2O_4$), doped with 2 wt% yttrium(III) oxide (Y_2O_3), is selected here for the 10-mm thick window to exploit its high strength (~4X of quartz glass), high fracture toughness[†] (>7X of quartz glass), and long-term resistance against creep and chemical corrosion at temperatures up to 2408 K (Ghosh et al., 2015; Liu et al., 2019), which qualified them as the prime candidate window material for high-energy laser applications subjected to hostile environments (Qadri et al., 2019; Sanghera et al., 2011). The optical transmittance of a 10-mm thick spinel varies between 0.8-0.86 across the 0.3-4.3 μm spectral band (Sepulveda et al., 2013), which is a wider transmittance range compared to other glazing materials (Dericioglu et al., 2005; Harris et al., 2013; Sanghera et al., 2011; Sanghera et al., 2015). Qadri et al., 2019 demonstrated that spinel transmittance can be enhanced up to 0.923 by using anti-reflective surface structures. Furthermore, the absorptance of spinel at 2000 K was found minimal (range average ~0.00262) at wavelengths <3 μm (Fernelius et al., 1982; Harris, 1998; Sako et al., 2021; Sanghera et al., 2011; Sova et al., 1998), which helps minimise the window cooling requirement. Minimising the absorptivity/emissivity at wavelengths >3 μm via application of infrared-reflective coatings is demonstrated viable and effective for windows, including a spinel window (Röger et al., 2009; Sanghera et al., 2011). The main disadvantage of using spinel is the high manufacturing costs, which could be minimised substantially by employing alternative fabrication techniques, such as processes proposed by Sanghera et al. (2015) and Villalobos et al. (2012).

3.3. Cavity wall configurations

Two cavity wall configurations are investigated to determine whether cavity walls should participate in solar absorption or remain reflective.

The first configuration is the 'reflective cavity' illustrated in Fig. 4(a). The HTF here is the sole absorber, while cavity wall interiors are lined with a highly reflective metallic coating to sustain the UHT operation. The rationale is that the high reflectance, combined with the large depth-to-aperture ratio of the cavity, will entrap most of the original solar input inside the cavity through internal reflections before being predominantly absorbed by the HTF. However, the requirement for highly reflective cavity walls could be a practical limitation due to reduced reflectance of metals at high temperatures (Garnov et al., 1997; Ujihara, 1972). Silver is the primary lining candidate, as it maintains specular reflectance >0.9 up to its melting point (1234.6 K) (Ujihara, 1972). For higher wall temperatures up to 2463 K, similar wall structure to the absorptive cavity may be used with a compatible reflective lining, such as zirconium-platinum (Alvey and George, 1991).

The second configuration is the 'absorptive cavity' illustrated in Fig. 4(b). The design comprises a tubular solar absorber attached to cavity walls to preheat the HTF before its direct solar absorption phase. Preheating, instead of post-heating, is used here to minimise the temperature of the solid absorber. The premise here is to use the exposed LM to attenuate the highly concentrated solar input by absorption and diffuse reflection. The weakened and diffusively reflected beams from the wavy film surface will then strike a larger absorbing area (cavity walls), hence, alleviating the material degradation concerns discussed in section 2.4 – this supposition will be verified in Part 3 by generating the incident radiation contours on internal walls using a radiation-coupled numerical solution. Furthermore, if hot spots are developed at the absorptive walls, their emissive radiation is less likely to escape from the cavity, given their small view factors with the aperture.

[†]Yb-doped $MgAl_2O_4$ maintains a fracture toughness >1.5 $MPa.m^{0.5}$ at 2073 K (Cao et al., 2013), which is more than double the fracture toughness of quartz glass at the room temperature (Bruns et al., 2020).

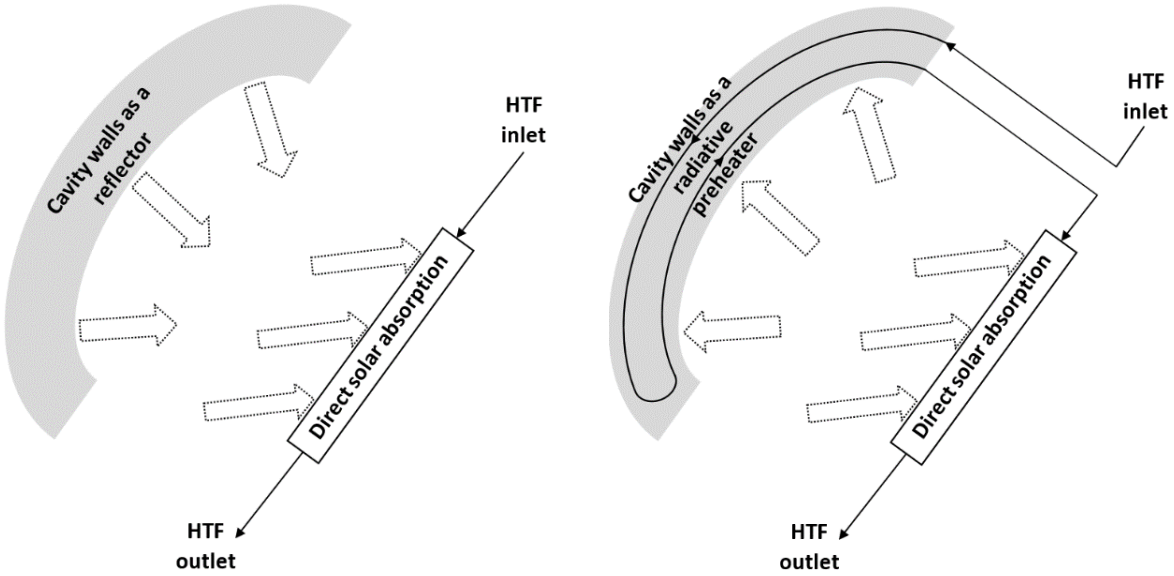

Fig. 4. Simplified schematics demonstrating the HTF flow routes at the two studied cavity wall configurations. (a) Reflective cavity, where solar absorption is handled solely by the HTF film. (b) Absorptive cavity, where the concentrated solar input is attenuated by the HTF film before reflecting to the cavity walls, which act as a preheater to the HTF.

Cavity walls are insulated by microporous insulation, which combines superior thermal properties with compactness at temperatures up to 1273 K (Unifrax, 2018). The absorptive cavity walls contain an additional, graphite-compatible, buffer insulation layer of zirconium oxide fibres to cover the temperature gradient down to 1273 K. Graphite coated with iron-cobalt-chromite spinel (Wang et al., 2021) can be used to build up the tubular absorber/preheater as shown in Fig. 5. Since the insulated cavity walls are subjected to trivial thermal loss to ambient, the absorbed energy by the walls are expected to require active cooling to protect the lining material from melting. The exposure of reflective walls to the metallic vapours at UHT may also deteriorate its performance, which requires further investigation before progressing with the reflective cavity configuration.

LMs are not recommended as efficient coolants for the reflective walls, given their high freezing points and low specific heat capacities. Therefore, a secondary fluid is likely to be used as a coolant for the reflective walls, which adds further complexity and inefficiencies. The cavity fluid can be a viable coolant (specific heat capacity >7X of liquid tin); however, direct recovery of its energy could be challenging. Circulating the cavity fluid from walls, and potentially the window and CPC, to the cavity would enable active control over the protective atmosphere inside the cavity. Contrary to the absorptive configuration, the coolant tubes/ducts will be embedded within the reflective walls, as shown in Fig. 5, to sustain their specularity. The effectiveness of different cooling mechanisms at each configuration is yet to be investigated.

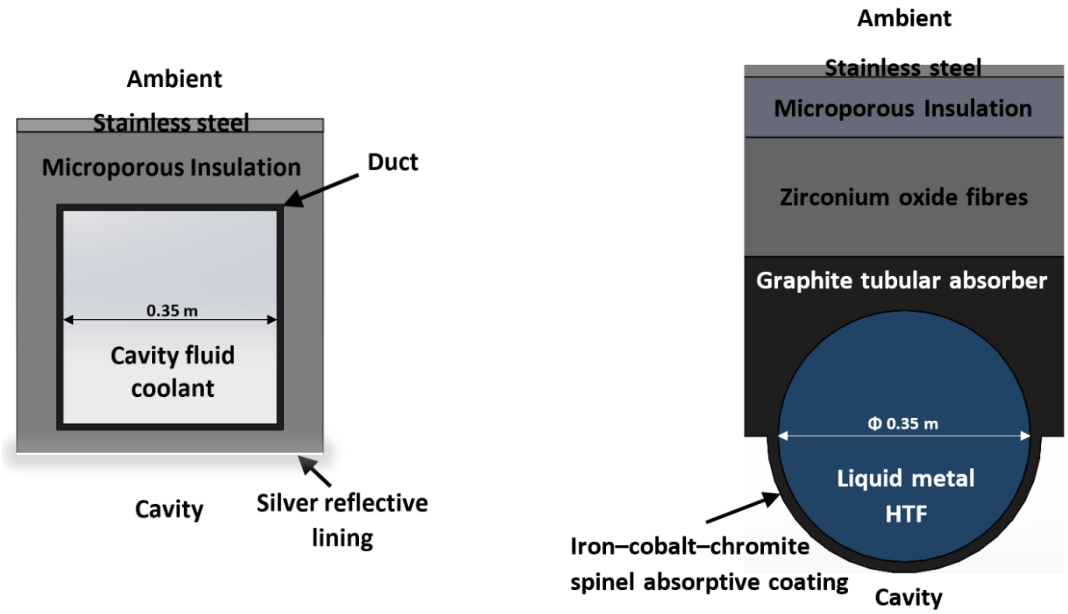

Fig. 5. Wall structures of the (a) reflective and (b) absorptive cavity configurations.

4. Energy model

An approximate quasi-steady-state energy model of the receiver is described and solved using the sequentially non-iterative approach to evaluate the receiver efficiency at each configuration. Model verification against a numerical solution will be presented in Part 3.

4.1. Assumptions

All internal cavity re-radiations are assumed diffuse to enable expressing the radiative transfer in terms of area ratios and view factors, which can be solved analytically. The diffuse assumption is particularly justified for rough graphite surfaces (Wang et al., 2014) and will be verified for the HTF film in Part 3 based on its surface waviness. Modelling the reflective walls as diffuse surfaces will be demonstrated in Part 3 as the primary source for the discrepancy of results against a reference numerical solution, due to underestimating the radiative losses from the reflective cavity; nevertheless, the maximum discrepancy was 5.7%. Therefore, the model is still considered a useful design tool, given its low computational requirements.

Window spectral selectivity is not considered in this analysis. Therefore, the model employs the grey radiation assumption, which is justified for the spinel window, given its stable transmittance at relevant spectral wavelengths as discussed in section 3.2. The solar source is treated as a blackbody thermal reservoir at 5200 K (Lovegrove and Pye, 2012). Accordingly, the optical properties are evaluated at the solar peak wavelength (λ_{sol}), which is calculated using Wein's displacement law:

$$\lambda_{sol} = 2898/T_{sun,bd} \tag{1}$$

where $T_{sun,bd}$ is the solar blackbody temperature.

Cavity walls are assumed adiabatic, as conduction is typically negligible compared to other heat transfer mechanisms at UHT (Becker and Vant-Hull, 1991). The conductive loss through the cavity walls may become significant when their effective thermal conductivity exceeds 0.1 $Wm^{-1}K^{-1}$

(DeAngelis et al., 2018). Here, the evaluated values are 0.031 $W.m^{-1}.K^{-1}$ and 0.092 $W.m^{-1}.K^{-1}$ for the reflective and absorptive cavity walls, respectively.

Cavity walls are assumed isothermal at 800 K and 1623.6 K for the reflective and absorptive configurations, respectively. The temperature of reflective walls should be kept as low as possible to maximise reflectance and minimise emissive losses. For the absorptive walls, their temperature should be higher than the desired HTF temperature after the preheat phase to account for the effectiveness of the wall heat exchanger (taken here as 90%). According to Ries et al. (1995), an isothermal cavity at 1673 K with at least two predefined temperature partitions – the cavity here has three temperature-defined partitions: HTF film, cavity walls, and window – is expected to underestimate the receiver efficiency by <6%. This underestimation inaccuracy tends to increase at temperatures closer to the equilibrium temperatures (3033.1 K at 6750 suns); hence, it is projected to be minimal for the <1000 K reflective cavity. Furthermore, this inaccuracy is likely to be small here, given the use of highly conductive wall materials (silver and graphite), which are also characterised by their insensitive reflectance/emissivities to temperature (Thorn and Simpson, 1953; Ujihara, 1972).

There is no available analytical steady-state solution for unstable film flowing over corrugated surfaces (Tseluiko et al., 2013), as Nusselt's solution (Nusselt, 1916) would overestimate the film thickness resulting in inaccurate velocity profiles when applied to wavy and turbulent films (Moran et al., 2002; Tseluiko et al., 2013; Yih, 1963). Therefore, the HTF film is modelled as an opaque and continuous frozen material with surface optical properties. Turbulence and continuity of the film flow will be numerically investigated in Part 2, where the geometrical properties of the corrugations will be demonstrated as a key factor in preserving the continuity. HTF thermo-physical and optical properties are evaluated at the mean flow temperature (1236.5 K), since variations of most tin properties at relevant temperatures are small (<5%) (Assael et al., 2010; Khvan et al., 2019). While deviations in the dynamic viscosity and thermal conductivity of molten tin from the mean temperature are more significant (<30%), these variations exhibited linear trends between 800 K and 1673 K; hence, a property value at the mean temperature is still justfied (Assael et al., 2010; Assael et al., 2017; Giordanengo et al., 1999). Similarly, the emissivity of molten tin is taken as 0.2289 (Greenstein, 1989). Wall emissivities were approximated as 0.1 for metallic reflective walls (Ramanathan and Yen, 1977) and 0.8 for graphite absorptive walls (Thorn and Simpson, 1953). The cavity fluid is modelled as an inert mixture (90 wt% N_2 and 10 wt% H_2) gas.

4.2. Model description

The maximum receiver efficiency ($\eta_{rec,max}$) is expressed by Steinfeld (2002) in terms of temperature (T) and average incident flux on the field (I_{field}):

$$\eta_{rec,max} = 1 - (\sigma T^4 / CR_g I_{field}) \tag{2}$$

where σ is Stefan-Boltzmann constant and CR_g is the geometric concentration ratio. $\eta_{rec,max}$ is 95.6% at $T = 1673$ K for a CR_g of 10,000 and I_{field} of 1000 Wm^{-2}. However, the actual efficiency (η_{rec}) would be lower, typically ranges between 45-80% (Le Roux, 2014; Maurya et al., 2022), due to additional energy losses. η_{rec} is defined here as:

$$\eta_{rec} = \dot{Q}_{abs} / P_{sol} = \dot{Q}_{abs} / (A_{ap} p_{sol}) \tag{3}$$

where $\dot{Q}_{abs}$ is the net (useful) rate of energy absorption/collection, A_{ap} the aperture area, P_{sol} and p_{sol} are the concentrated solar power and flux impinging the external surface of the aperture window, respectively. P_{sol} is given as:

$$P_{sol} = \eta_o \int_{\lambda=0}^{\infty} \int_{A_{helio}} \int_{\Omega=0}^{2\pi} I_{\lambda,sol}(\hat{\boldsymbol{r}}, \lambda, \hat{\boldsymbol{s}}) \, |\hat{\boldsymbol{n}}.\hat{\boldsymbol{s}}| \, d\Omega dA d\lambda$$
$$= \eta_o A_{helio} \left[\int_{\Omega=0}^{2\pi} I_{sol}(\hat{\boldsymbol{r}}, \hat{\boldsymbol{s}}) \, |\hat{\boldsymbol{n}}.\hat{\boldsymbol{s}}| d\Omega \right]_{\lambda=\lambda_p} \quad (4)$$

where A_{helio} is heliostats aperture area, Ω the solid angle, $I_{sol}(\hat{\boldsymbol{r}}, \hat{\boldsymbol{s}})$ the incident solar radiation on an elemental heliostat area with a position vector $\hat{\boldsymbol{r}}$ and normal $\hat{\boldsymbol{s}}$, and η_o the overall optical efficiency. The optical efficiencies of the polar-field and CPC are taken as 75% (Rinaldi et al., 2014) and 90% (Li. et al., 2019), respectively, which result in η_o of 67.5%. Therefore, the optical concentration ratio (CR_o) and p_{sol} could be expressed as:

$$CR_o = \eta_o (A_{helio}/A_{ap}) = \eta_o CR_g \quad (5)$$

$$p_{sol} = CR_o \left[\int_{\Omega=0}^{2\pi} I_{sol}(\hat{\boldsymbol{r}}, \hat{\boldsymbol{s}}) \, |\hat{\boldsymbol{n}}.\hat{\boldsymbol{s}}| d\Omega \right]_{\lambda=\lambda_p} \approx CR_o I_{field} \quad (6)$$

P_{sol} is attenuated by the window before incurring emissive ($\dot{Q}_e$), reflective ($\dot{Q}_{ref}$), and natural convective ($\dot{Q}_c$) losses inside the cavity. The unrecovered energy absorbed by the walls is also accounted as a loss. Thus, $\dot{Q}_{abs}$ is expressed as:

$$\dot{Q}_{abs} = \tau_{win} P_{sol} - \dot{Q}_e - \dot{Q}_{ref} - \dot{Q}_c - (1 - \eta_{rv})\dot{Q}_w - \dot{Q}_{win,int} = \dot{Q}_{abs,htf} + \eta_{rv}\dot{Q}_w \quad (7)$$

where τ_{win} is the window transmittance (taken as 0.86), $\dot{Q}_{win,int}$ the window internal absorption, $\dot{Q}_{abs,htf}$ the HTF film absorption, $\dot{Q}_w$ the wall absorption, and η_{rv} the recovered energy fraction from walls, which is zero for the reflective cavity and taken as 0.9 for the absorptive preheater based on efficiencies of existing LM tubular heat exchangers (Sandia, 1983; Schiel and Geyer, 1988). In theory, η_{rv} could be >0 in the reflective cavity if energy extracted by the coolant is recovered; however, its temperature is unlikely to be sufficiently higher than the HTF inlet to facilitate an effective heat transfer.

Considering a continuous HTF film, its mass flow rate ($\dot{m}$) and film thickness at location x ($t_{|x}$) can be estimated from:

$$\dot{m} = \dot{Q}_{abs}/(c_P \Delta T) \quad (8)$$

$$t_{|x} = \dot{m}/(w\rho v_{|x}) \quad (9)$$

where ΔT is temperature difference between HTF inlet and outlet, $v_{|x}$ the flow velocity at location x, and w the internal width of receiver, c_P and ρ are specific heat capacity and density of the HTF, respectively.

4.2.1. Emission

Radiative losses are composed of emissive and reflective components escaping from the cavity through the aperture. To evaluate the emissive loss, the internal cavity area (A_{cav}) is discretised into a finite number (n) of planar surfaces, where each surface is labelled with an index i and has a defined surface area (A_i), temperature (T_i), emissivity (ϵ_i), and a view factor towards the aperture (F_{i-ap}). Therefore, by utilising the grey and diffuse assumptions, the summation and reciprocity rules can be used to evaluate the net emissive transfer at the aperture from other surfaces of the enclosure as (Incropera et al., 2017):

$$\dot{Q}_e = \tau_{win}\sigma A_{ap}\sum_{i=1}^{n-1}\frac{{T_i}^4 - {T_a}^4}{\frac{1-\epsilon_i}{A_i\epsilon_i} + \frac{1}{A_i F_{i-ap}}} \tag{10}$$

where T_a is ambient temperature. By substituting with the mean HTF and isothermal wall temperatures and emissivities, equation 10 becomes:

$$\dot{Q}_e = \tau_{win}\sigma A_{ap}\left[\frac{{T_{htf}}^4 - {T_a}^4}{\frac{1-\epsilon_{htf}}{A_{htf}\epsilon_{htf}} + \frac{1}{A_{htf}F_{htf-ap}}} + ({T_w}^4 - {T_a}^4)\sum_{i=1}^{n-2}\frac{1}{\frac{1-\epsilon_w}{A_i\epsilon_w} + \frac{1}{A_i F_{i-ap}}}\right] \tag{11}$$

where htf and w subscripts denote the HTF film and cavity walls, respectively. The view factors are computed using a MATLAB code by Lauzier (2004) based on the contour double integral formulation, which is verified for complex geometries (Francisco et al., 2014), with vertices coordiantes imported from the CAD model.

4.2.2. Reflection

Reflective loss transmitted through the window can be expressed in terms of geometrical and optical parameters as (Duffie et al., 1985; Zou et al., 2017):

$$\dot{Q}_{ref} = \left[1 - \frac{\epsilon_{cav}}{1-(1-\epsilon_{cav})\,(1-A_{ap}/A_{cav})}\right]\tau_{win}^2 P_{sol} \tag{12}$$

where ϵ_{cav} is an effective cavity emissivity approximated by area-weighted averaging of HTF (ϵ_{htf}) and cavity wall lining (ϵ_w) emissivities:

$$\epsilon_{cav} = (1/A_{cav})\sum_{i=1}^{n}\epsilon_i\left(A_i F_{i-ap}\right) = (1/A_{cav})\left[\epsilon_{htf}A_{htf}F_{htf-ap} + \epsilon_w\sum_{i=1}^{n-1}\left(A_i F_{i-ap}\right)\right] \tag{13}$$

The transmitted solar input is not diffuse; hence, the first absorption instance by the HTF film ($\dot{Q}_{htf,1st}$) and cavity walls ($\dot{Q}_{w,1st}$) are evaluated as:

$$\dot{Q}_{htf,1st} = (1-x)\epsilon_{htf}\tau_{win}P_{sol} \tag{14}$$

$$\dot{Q}_{w,1st} = x\epsilon_w \tau_{win} P_{sol} \tag{15}$$

where x is the fraction of transmitted solar radiation striking the walls instead of the HTF film. This fraction depends on the refractive index of the window, distribution and directional vector of the incident solar beams on the window, and cavity width. x can be evaluated using the discrete ordinates model, as will be demonstrated in Part 3.

Secondary (internal) reflections of the solar input is assumed diffuse, defined here as internal reflections occurring after the solar input strikes any internal surface once, are assumed diffuse. The total absorption from the secondary reflections ($\dot{Q}_{abs,2nd}$) is evaluated by subtracting the initial absorption instances from the total absorption:

$$\dot{Q}_{abs,2nd} = \dot{Q}_{abs} - (\dot{Q}_{htf,1st} + \dot{Q}_{htf,1st}) \tag{16}$$

Internal window reflections ($\dot{Q}_{win,ref}$) are expressed as:

$$\dot{Q}_{win,ref} = (1 - \tau_{win} - \epsilon_{win}) \frac{\dot{Q}_{ref} + \dot{Q}_e}{\tau_{win}} \tag{17}$$

where ϵ_{win} is window emissivity. Given the small $\dot{Q}_{win,ref}$ quantities (0.9-2.2% of input power), it is assumed to be completely absorbed by the internal surfaces.

4.2.3. Absorption

Utilising the diffuse re-radiation assumption, $\dot{Q}_{abs,2nd}$ and $\dot{Q}_{win,ref}$ are distributed on the HTF and walls weighted by each's surface area and emissivity as:

$$\dot{Q}_{abs,htf} = \dot{Q}_{htf,1st} + \frac{\epsilon_{htf} A_{htf}}{\epsilon_{htf} A_{htf} + \epsilon_w A_w} \left(\dot{Q}_{abs,2nd} + \dot{Q}_{win,ref}\right) \tag{18}$$

$$\dot{Q}_w = \dot{Q}_{w,1st} + \frac{\epsilon_w A_w}{\epsilon_{htf} A_{htf} + \epsilon_w A_w} \left(\dot{Q}_{abs,2nd} + \dot{Q}_{win,ref}\right) \tag{19}$$

The total window absorption ($\dot{Q}_{win}$) is evaluated using:

$$\dot{Q}_{win} = \epsilon_{win} P_{sol} + \dot{Q}_{win,int} = \epsilon_{win} (P_{sol} + \frac{\dot{Q}_{ref} + \dot{Q}_e}{\tau_{win}}) \tag{20}$$

4.2.4. Convection

For an insulated and windowed cavity, wind-induced convection is considered an indirect loss mechanism, which discharges the energy lost through window absorption. Therefore, the wind-induced convection loss is implicit within the $\tau_{win} P_{sol}$ and $\dot{Q}_{win,int}$ terms in Equation 7, while the natural convection loss is represented explicitly using the $\dot{Q}_c$ term.

The convective heat transfer coefficient (h) of any domain surface is defined as:

$$h = (Nu\, k_{cav})/L_{ch} \tag{21}$$

where k_{cav} is the thermal conductivity of cavity fluid, L_{ch} the characteristic length, and Nu the Nusselt number, which is related to Rayleigh number (Ra) via:

$$Nu = c(Ra)^n \tag{22}$$

where c and n are constants describing the geometry/orientation of the absorbing surface(s) and flow regime, respectively. Constants for different shapes, orientations, flow regimes, and fluids are available in literature (Aydın and Guessous, 2001; Becker and Vant-Hull, 1991; Bennett, 1974; Tsuji and Nagano; 1988). Interaction effects between surface radiation and turbulent natural convection are negligible (variations in Nu values <1%) for rectangular enclosures with aspect ratios >3 (Velusamy et al., 2001); hence, Nu is acquired from a decoupled correlation. Constants for rectangular enclosures with inclined surface(s) are provided by Catton (1978). For open-aperture cavities, Samanes et al. (2014) recommends Clausing (1983). Different literature correlations will be compared against a CFD solution to examine their validity in Part 3.

The calculated Ra values were 256×10^9 and 1.24×10^7 for the reflective and absorptive cavities, respectively. Therefore, for a cavity fluid with a Prandtl number ~0.76, the buoyancy-driven flow is considered fully turbulent in both configurations (Krishnamurti, 1973). Please note that no empirical correlation or analytical expression is available to model the interfacial shearing effects on natural convection. In Part 2, a CFD solution is used to demonstrate the insignificance of such viscous effects on the bulk flow.

The convective loss per configuration is based on the temperature(s) and convective heat transfer coefficient(s) of its respective absorbing surface(s):

$$\dot{Q}_{c,reflective} = A_{htf} h_{htf} \left(T_{htf} - T_{cav}\right) \tag{23}$$

$$\dot{Q}_{c,absorptive} = A_{htf} h_{htf} \left(T_{htf} - T_{cav}\right) + A_w h_w (T_w - T_{cav}) \tag{24}$$

where T_{cav} is an effective cavity temperature calculated as:

$$T_{cav} = (1/A_{cav})(T_{htf} A_{htf} + T_w A_w + T_{win} A_{ap}) \tag{25}$$

where T_{win} is the window temperature.

5. Results and discussion

The energy performance of the proposed receiver is presented to investigate its feasibility and study the influence of selected parameters on its energy efficiency.

5.1. Energy flow

The power flow for each cavity configuration is presented in Fig. 6. The overall efficiency of the absorptive cavity is 74% compared to only 31.9% for the reflective cavity. While the latter was successful in entrapping >80% of transmitted solar radiation into the cavity, more than half of this energy was absorbed by the walls despite their high reflectance. This is a result of the large walls-to-film area ratio (~4.66), as 52% of all secondary reflections were absorbed by the walls. The absorptive cavity captured >90% of the transmitted radiation with <8% unrecovered energy from the walls. While the emissive loss was 4X greater in the absorptive cavity due to its higher temperature and effective emissivity, the total re-radiative losses from its aperture were ~60% lower than in the reflective cavity due to the latter's substantial reflective loss.

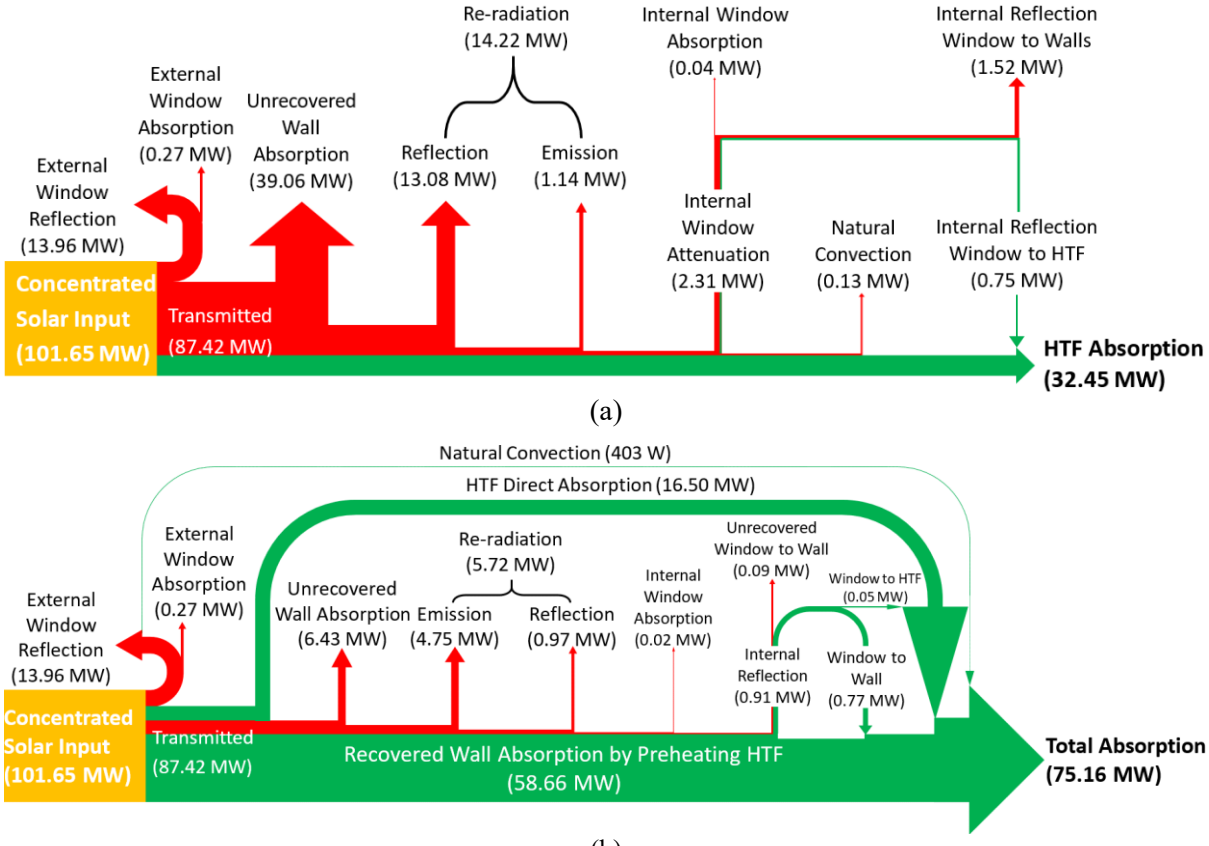

Fig. 6. Rate of energy flow throughout the (a) reflective and (b) absorptive cavities. Colour convention: red marks losses; green marks energy collection; orange marks input.

The significant wall absorption marks a vital conceptual concern for the reflective cavity, as walls necessitate active cooling to discharge over 38% of the solar input. A full recovery of this energy may boost the efficiency up to 70.3%, which would still be less efficient than its absorptive counterpart. In practice, a full, or even sizeable, recovery from the reflective walls is unlikely, as discussed in section 3.3. Nevertheless, instead of direct energy recovery during nominal operation, heat collected by the coolant could be utilised in preserving the HTF above its melting point. Assuming 80% efficient heat

transfer from the reflective walls to cavity fluid for 6h (sun hours) and 80% efficient heat transfer to the stored liquid tin for 18h (night-time hours), the resultant energy can cover temperature drops up to 225 K at the studied scale. This limitation could be minimised by maximising the wall reflectance and the HTF emissivity. The influences of these two optical properties are addressed in sections 5.4 and 5.5.

5.2. Concentration ratio

Solar concentration is essential at UHT to minimise the energy losses from the aperture. However, beyond an optimal concentration ratio, further concentration might not save sufficient energy to outweigh the increased spillage and CPC losses. To model this effect, η_o was linearly varied from 75% to 55% to correspond to an increasing CR_o from 1 sun to 20,000 suns, respectively. As indicated in Fig. 7, concentration ratios >1000 suns are more justifiable at UHT for an absorptive cavity than a reflective cavity.

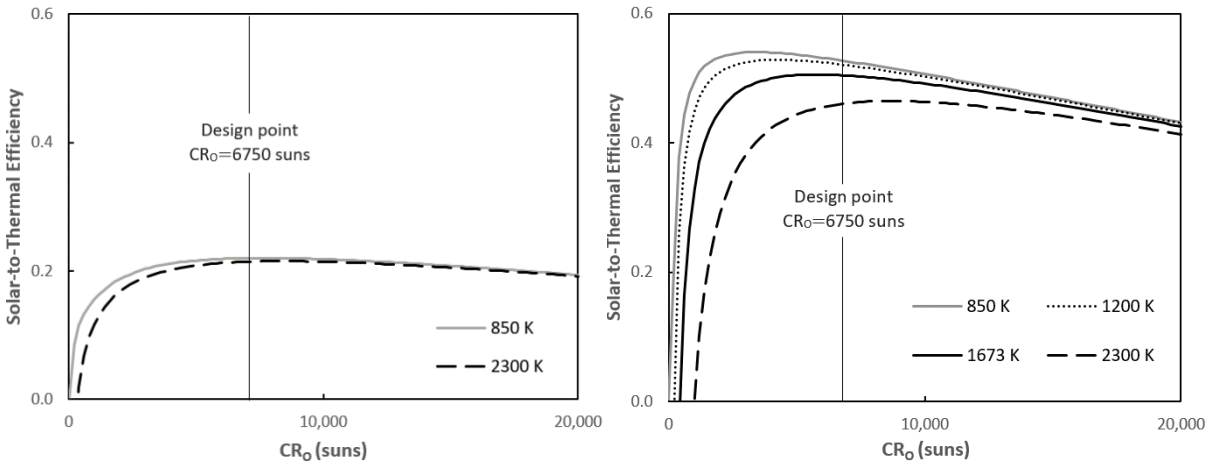

Fig. 7. Effect of optical concentration ratio (CR_O) on the solar-to-thermal efficiency at different temperatures. in the (a) reflective and (b) absorptive cavities. The plots shows that the higher the temperature, the more substantial efficiency gains could be achieved by increasing the concentration ratio. However, temperature seems to have trivial influence on the on the optimal concentration ratio of the reflective cavity. Please note that the wall temperature in the reflective cavity cases is maintained at 800 K, while it varied in the absorptive cavity cases with the receiver temperature, as walls in the latter participate in the energy absorption. Wall temperature is uncoupled from the concentration ratio, which is justified by the active cooling of walls in both configurations.

5.3. Natural convection

Natural convection was found to pose an opposite effect per cavity configuration (Table 4). The cold reflective walls resulted in a lower cavity temperature than the mean HTF film temperature; hence, the resultant buoyancy-driven effect inside the cavity is the extraction of heat from the HTF film. In the absorptive cavity, the temperatures of the absorbing surfaces, HTF film and walls, are lower than the cavity temperature; therefore, the resultant buoyancy-driven effect is conveying heat from the window to the absorbing surfaces. The latter mechanism is favourable, as it passively provides heat recovery from, and cooling to, the window. Nevertheless, the convective magnitude of this mechanism is minor in the absorptive cavity due to the small temperature differences across its domain.

Table 4
Calculated temperatures and convection heat transfer coefficients.

Configuration	Reflective	Absorptive
T_{abs} (K)	1236.5	1614.9
T_{win} (K)	2089.09	2182.05
T_{cav} (K)	910.4	1628.7
h_{abs} (W.m^{-2}.K^{-1})	1.1577	-0.0105*

*The negative sign indicates an opposite heat transfer (energy gain by the absorbing surfaces) due to T_{cav}>T_{abs}.

The influence of h_{abs} on the overall receiver efficiency is demonstrated in Fig. 8. A typical h_{abs} value in a buoyancy-dominated cavity ranges between 1-15 Wm^{-2}K^{-1} (DeAngelis et al., 2018), which may become slightly higher when accounting for the interfacial shearing effects. If viscous effects are ignored, h_{abs} would depend on the temperature difference across the domain ($T_{abs} - T_{cav}$). Accordingly, natural convection posed a more significant impact on the reflective cavity efficiency at higher temperatures, as shown in Fig. 8(a). Since the favourable convective mechanism in the absorptive cavity occurs only when the cavity is at a lower temperature than the window, this effect, resembled by the positive slope in Fig. 8(b), diminishes at higher receiver temperatures before becoming a loss mechanism at temperatures >T_{win}. Overall, natural convection is shown to pose minimal influence on the efficiency of a windowed cavity receiver.

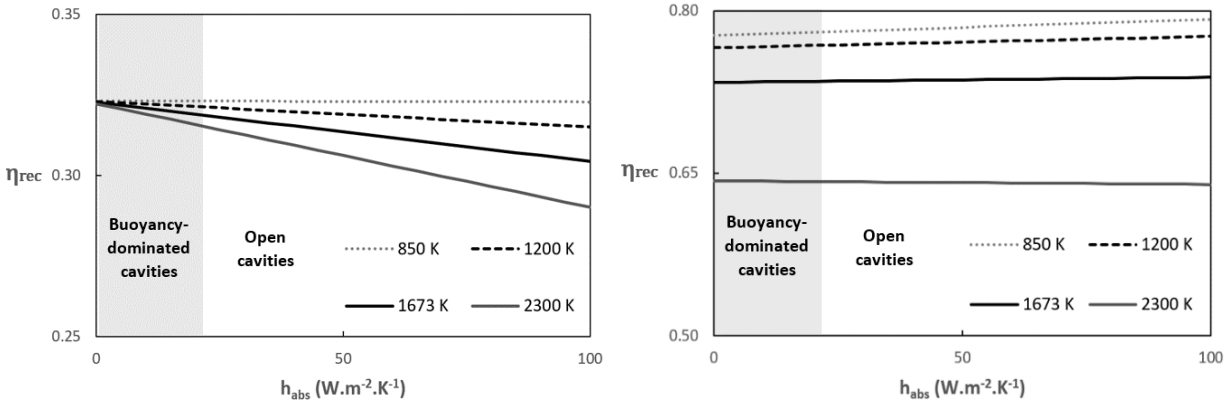

Fig. 8. Effect of convection heat transfer coefficient (h_{abs}) on the receiver efficiency at different HTF outlet temperatures in the (a) reflective and (b) absorptive cavities. h_{abs} is presented here as an absolute quantity, which explains the trends with positive slopes, where heat is transferred to, rather than from, the absorbing surfaces.

5.4. Window temperature

The quasi-steady-state window temperature is estimated by equating the total window absorption to the emissive and convective losses from the window using the parameters displayed in Table 5. In Part 3, the volumetric optical properties of spinel and the discrete ordinates method will be used to verify these results.

The evaluated temperatures of the passive-cooled window are below the maximum allowable temperature specified in section 3.2 as 2408 K. Nevertheless, the window is likely to necessitate active cooling to factor in the transient heating/cooling. For zero allowable strain, the thermal stress (σ_{th}) can be estimated using:

$$\sigma_{th} = E\delta\Delta T_{win} \tag{26}$$

where E is Young's Modulus (282 GPa) and δ the thermal expansion coefficient (5.9×10^{-6} K^{-1}). For spinel's fracture strength of 350 MPa (Sanghera et al., 2011), the active cooling should keep the transient ΔT_{win} <200 K. The utilisation of cavity fluid as window coolant is yet to be investigated.

Table 5
Evaluated parameters used to estimate the quasi-steady-state window temperature.

Configuration	Reflective	Absorptive
T_a (K)	300	300
T_{cav} (K)	910.4	1628.7
Wind speed ($m.s^{-1}$)	3	3
h_{wind} ($W.m^{-2}.K^{-1}$)	6.4809	6.4809
h_{win} ($W.m^{-2}.K^{-1}$)	2.726	0.1642
Total window absorption (kW)	309.64	283.74
Total convective loss from window (kW)	224.33	197.49
Total emissive loss from window (kW)	85.31	86.25
T_{win} (K)	2089.09	2182.05

5.5. Liquid metal emissivity

The HTF emissivity was varied to determine its influence on the receiver efficiency (Fig. 9). Results are compared with data from DeAngelis et al. (2018) of a tubular LM receiver at 1623 K. Overall, the HTF emissivity was found to influence the performance of the reflective cavity more than the absorptive cavity. The absorptive receiver exhibited comparable efficiencies to the reference receiver.

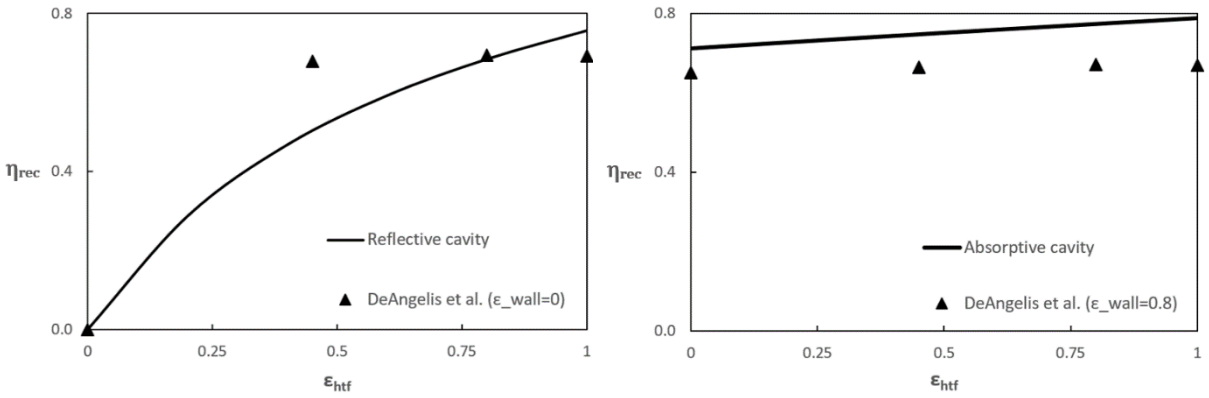

Fig. 9. Effect of HTF emissivity (ϵ_{htf}) on the receiver efficiency in the (a) reflective and (b) absorptive cavities. The emissivity values of DeAngelis et al. (2018) data are based on the emissivity of the absorber tubes instead of optically exposed HTF.

Increasing the HTF emissivity in the reflective cavity from 0.2289 to 0.85 can substantially reduce energy wasted through cavity walls by 78%, while improving the solar entrapment by 9%, as illustrated in Fig. 10. Still, the collected energy remains lower than the absorptive cavity without a modified HTF emissivity.

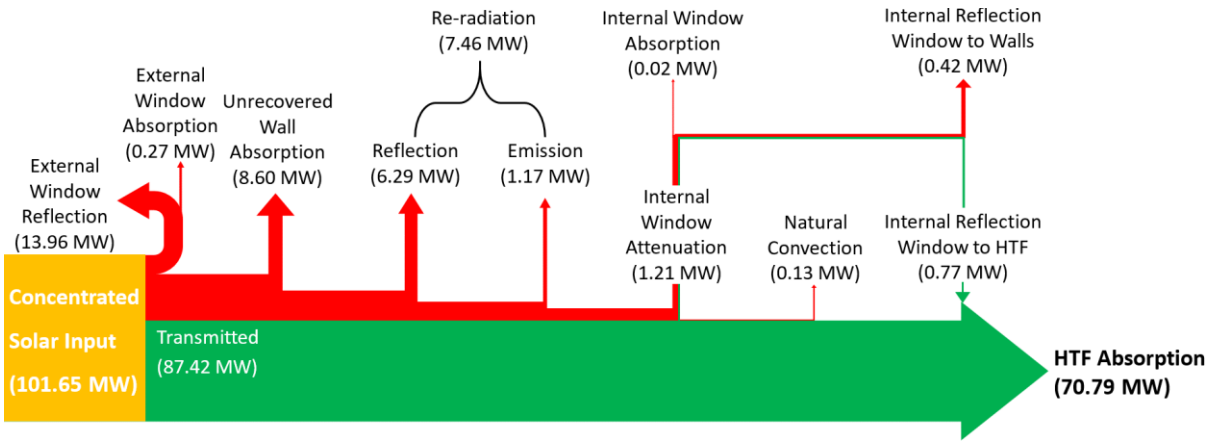

Fig. 10. Energy flow diagram through the reflective cavity with an improved HTF emissivity of 0.85. Colour convention: red marks losses routes; green marks collection routes. Colour convention: red marks losses; green marks energy collection; orange marks input.

5.6. Wall reflectance

The wall reflectance $(1-\epsilon_w)$ has an opposite effect on the performance of each cavity configuration, as demonstrated in Fig. 11. Regardless of the configuration, this effect is minimal at wall reflectance <0.8 but becomes dramatically significant at higher reflectance. This highlights the importance of maximising wall reflectance in the reflective cavity, whereas wall optical properties are less critical for the absorptive cavity. The reflectivity of silver, at 0.69 μm, drops from 0.972 to 0.939 when temperature increases from 800 K to 1234 K (Ujihara, 1972), which, from Fig. 11, corresponds to decreased reflective receiver efficiency of ~8%. However, this impact can be considerably higher for other lining metals (Ujihara, 1972), which emphasises the importance of preserving the reflective walls at the lowest possible temperature.

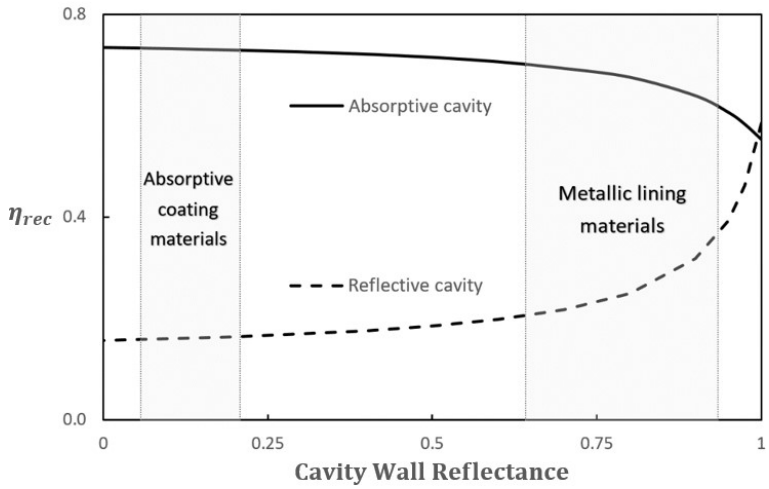

Fig. 11. Effect of cavity wall reflectance on the receiver efficiency at both cavity configurations.

6. Conclusion

A new UHT receiver concept was proposed featuring an optically exposed LM HTF to mitigate previous concerns about subjecting solid absorbers to concentrated irradiation. The concept is theoretically investigated for heating liquid tin from 800 K to 1673 K, at two possible cavity configurations, using an approximate quasi-steady-state energy model. The presented design and modelling methodology may be generalised for broad receiver analysis.

The main findings are summarised as follows:

1. Using a LM as the sole absorber in a reflective cavity would result in poor efficiencies (<40%) attributed to the substantial wall absorption and reflective loss. Higher efficiencies (>70%) are attainable by employing the LM film as an internal reflector/moderator to the concentrated solar input, while the majority of absorption is handled by the absorptive cavity via radiative wall absorber.

2. Reflective cavity efficiency is found more sensitive to the internal optical properties than the absorptive cavity. While some measures were proposed to alleviate this limitation, it would still be less efficient than an equivalent absorptive cavity.

3. Reflective cavity walls require lining with a highly reflective and thermally resistant material, which may be unachievable, as metallic reflectance deteriorate with temperature. Preserving reflectance at UHT, and under exposure to corrosive metal vapours, necessitate substantial cooling. While using the LM HTF as a coolant is found unfeasible, the cavity fluid is projected to be an effective alternative; yet, energy recovery is unlikely to be as efficient as in the absorptive cavity.

4. Sealing the cavity aperture is required to protect against oxidising ambient effects. A transparent ceramic window was proposed to exploit its superior thermo-mechanical and optical properties at UHT compared to conventional glazing materials. Preliminary qualitative and quantitative (thermal analysis) assessments demonstrated its potential and challenges, including requirement for active cooling. Further investigations are still required to determine its practical feasibility at large-scales. While currently underdeveloped for this application, fluidic seals may eventually become an optically efficient alternative to windows.

5. At UHT, increasing concentration ratios beyond 1000 suns is particularly advantageous for absorptive cavity receivers.

6. Natural convection is unlikely to pose any significant influence on the energy performance of the windowed receiver.

Some practical and operational challenges were emphasised and conceptually addressed, including manufacturing of the components and energy recovery from the walls. The proposed measures are yet to be practically investigated. In Parts 2 and 3, a transient radiation-CFD coupled analysis will be described to verify the results and appraise the employed assumptions of the presented analytical model. The promising performance of the absorptive cavity prompts performing a techno-economic and environmental analysis to justify or improve the suggested design selections made in this paper for a particular UHT application, such as a thermochemical process.

Acknowledgment

The authors would like to thank the reviewers at the Solar Energy journal for their valuable feedback and insights. This research was funded by the University of Edinburgh Principal's Career Development Scheme and Edinburgh Global. For the purpose of open access, the author has applied a Creative Commons Attribution (CC BY) licence to any Author Accepted Manuscript version arising from this submission.

References

Ahmad, S.Q.S., Wieckert, C. and Hand, R.J., 2017. Glass melting using concentrated solar thermal energy. Glass Techno.: Eur. J. of Glass Sci. and Techno.: Part A 58(2), 41–48.

Alipourtarzanagh, E., Chinnici, A., Nathan, G.J., Dally, B.B., 2020. Experimental insights into the mechanism of heat losses from a cylindrical solar cavity receiver equipped with an air curtain. Sol. Energy 201, 314-322.

Alvey, M. D., George, P.M., 1991. ZrPt3 as a high-temperature, reflective, oxidation-resistant coating for carbon-carbon composites. Carbon 29(4), 523-530.

Ambrosetti, G., Good, P., 2019. A novel approach to high temperature solar receivers with an absorbing gas as heat transfer fluid and reduced radiative losses. Sol. Energy 183, 521-531.

Amy, C., Budenstein, D., Bagepalli, M., England, D., DeAngelis, F., Wilk, G., Jarrett, C., Kelsall, C., Hirschey, J., Wen, H., Chavan, A., Gilleland, B., Yuan, C., Chueh, W.C., Sandhage, K.H., Kawajiri, Y., Henry, A., 2017. Pumping liquid metal at high temperatures up to 1,673 kelvin. Nature 550, 199–203.

Amy, C., Seyf, H.R., Steiner, M.A., Friedman, D.J., Henry, A., 2019. Thermal energy grid storage using multi-junction photovoltaics. Energy Environ. Sci. 12, 334-343.

Arrif, T., Benchabane, A., Guermoui, M., Gama, A. and Merarda, H., 2021. Optical performance study of different shapes of solar cavity receivers used in central receiver system plan. Int. J. of Ambient Energy 42(1), 81-95.

Assael, M.J., Chatzimichailidis, A., Antoniadis, K.D., Wakeham, W.A., Huber, M.L., Fukuyama, H., 2017. Reference correlations for the thermal conductivity of liquid copper, gallium, indium, iron, lead, nickel and tin. High temperatures. High pressures 46(6), 391-416.

Assael, M.J., Kakosimos, K., Banish, R.M., Brillo, J., Egry, I., Brooks, R., Quested, P.N., Mills, K.C., Nagashima, A., Sato, Y., Wakeham, W.A., 2006. Reference Data for the Density and Viscosity of Liquid Aluminum and Liquid Iron. J. of Physical and Chemical Reference Data 35**,** 285-300.

Assael, M.J., Kalyva, A.E., Antoniadis, K.D., Michael Banish, R., Egry, I., Wu, J., Kaschnitz, E., Wakeham, W.A., 2010. Reference Data for the Density and Viscosity of Liquid Copper and Liquid Tin. J. of Physical and Chemical Reference Data 39(3), 033105.

Ávila-Marín, A.L., 2011. Volumetric receivers in solar thermal power plants with central receiver system technology: a review. Sol. Energy 85**,** 891-910.

Aydın, O., Guessous, L., 2001. Fundamental correlations for laminar and turbulent free convection from a uniformly heated vertical plate. Int. J. of Heat and Mass Transfer 44**,** 4605-4611.

Becker, K., Hofmann, A., Hünermann, M., Schenk, C., 2013. Solar radiation receiver having an entry window made of quartz glass and method for producing an entry window. European Patent Office, EP2756237A1.

Becker, M., Vant-Hull, L.L., 1991. Thermal Receivers, in: Solar Power Plants: Fundamentals, Technology, Systems, Economics. Springer Berlin Heidelberg, Berlin, Heidelberg, pp. 163-198.

Bennett, C.O., 1974. Momentum, heat, and mass transfer, Second ed. McGraw-Hill, New York.

Bruns, S., Petho, L., Minnert, C., Michler, J., Durst, K., 2020. Fracture toughness determination of fused silica by cube corner indentation cracking and pillar splitting. Materials & Design 186, 108311.

Cao, W., Kundu, A., Yu, Z., Harmer, M.P., Vinci, R.P., 2013. Direct correlations between fracture toughness and grain boundary segregation behavior in ytterbium-doped magnesium aluminate spinel. Scripta Materialia 69(1), 81-84.

Catton, I. 1978. Natural convection in enclosures. In: Proceedings of the Int. Heat Transfer Conference, vol. 6, pp. 13–31.

Charpentier, L., Balat-Pichelin, M., Sciti, D., Silvestroni, L., 2012. High temperature oxidation of carbides UHTC in air. In: Proceedings of the 8th Int. Symposium On High-Temperature Corrosion and Protection of Materials, HAL-02313863, Les Embiez, France.

Clausing, A.M., 1983. Convective losses from solar central receivers – comparisons between analytical predictions and experimental results. J. Sol. Energy Eng., 105, 29-33.

Çengel, Y.A., 2019. Thermodynamics: an engineering approach, Ninth ed. McGraw-Hill Education, New York.
Dahlioui, D., Wette, J., Fernández-García, A., Bouzekri, H., Azpitarte, I., 2022. Performance assessment of the anti-soiling coating on solar mirrors soiling in the arid climate of Ouarzazate-Morocco. Sol. Energy 241, 13-23.
Datas, A., 2021. Ultra-high temperature thermal energy storage, transfer and conversion, Woodhead Publishing, Duxford.
DeAngelis, F., Seyf, H.R., Berman, R., Schmidt, G., Moore, D., Henry, A., 2018. Design of a high temperature (1350 °C) solar receiver based on a liquid metal heat transfer fluid: Sensitivity analysis. Sol. Energy 164**,** 200-209.
Deng, Y., Jiang, Y., Liu, J., 2021. Liquid metal technology in solar power generation - Basics and applications. Sol. Energy Materials and Sol. Cells 222, 110925.
Dericioglu, A.F., Boccaccini, A.R., Dlouhy, I., Kagawa, Y., 2005. Effect of chemical composition on the optical properties and fracture toughness of transparent magnesium aluminate spinel ceramics. Materials Transactions 46**,** 996-1003.
Diago, M., Iniesta, A., Soum-Glaude, A., Calvet, N., 2018. Characterization of desert sand to be used as a high-temperature thermal energy storage medium in particle solar receiver technology. Appl. Energy 216**,** 402-413.
Dubrovinsky L.S., Saxena S.K., 1999. Emissivity measurement on some metals and oxides using multiwavelength spectral radiometry. HTHP 31, 393–9.
Duffie, J.A., Beckman, W.A., McGowan, J., 1985. Solar engineering of thermal processes. American J. of Physics 53**,** 382-382.
Erickson, L., Gavilan, A., 2014. Optically transparent single-crystal ceramic receiver tubes for concentrated solar power, WIPO (PCT), WO2014149261A1.
Fang, J., Tu, N., Wei, J., 2014. Effects of absorber emissivity on thermal performance of a solar cavity receiver. Advances in Condensed Matter Physics 2014(4), 1-10.
Fernelius, N.C., Coble, G.S., Dempsey, D.V., Detrio, J.A., Fox, J.A., Greason, P.R., Johnston, G.T., O'Quinn, D.B., 1982. Multiwavelength laser rate calorimetry on various infrared window materials. In: Proceedings of the 25th Annual Technical Symposium, Emerging Opt. Materials, vol. 0297, pp. 137-142.
Flesch, R., Stadler, H., Uhlig, R. and Pitz-Paal, R., 2014. Numerical analysis of the influence of inclination angle and wind on the heat losses of cavity receivers for solar thermal power towers. Sol. Energy 110, 427-437.
Fletcher, E.A., 2001. Solarthermal processing: a review. J. Sol. Energy Eng. 123, 63-74.
Francis, L.F., 2016. Melt Processes, in: Materials Processing. Academic Press, Boston, pp. 105-249.
Francisco, S.C., Raimundo, A.M., Gaspar, A.R., Oliveira, A.V.M., Quintela, D.A., 2014. Calculation of view factors for complex geometries using Stokes' theorem. J. of Building Performance Simulation 7(3), 203-216.
Frazer, D., Stergar, E., Cionea, C., Hosemann, P., 2014. Liquid metal as a heat transport fluid for thermal solar power applications. Energy Procedia 49, 627-636.
Frignani, M., Alemberti, A., Tarantino, M., 2019. ALFRED: A revised concept to improve pool related thermal-hydraulics. Nuclear Eng. and Design 355, 110359.
Fritsch, A., Flesch, J., Geza, V., Singer, C., Uhlig, R., Hoffschmidt, B., 2015. Conceptual study of central receiver systems with liquid metals as efficient heat transfer fluids. Energy Procedia 69, 644-653.
Garnov, S.V., Konov, V.I., Tsarkova, O.G., Dausinger, F., Raiber, A., 1997. High-temperature measurements of reflectivity and heat capacity of metals and dielectrics at 1064 nm. Laser-Induced Damage in Opt. Materials 2966, 149-156.
Ghosh, C., Ghosh, A., Haldar, M.K., 2015. Studies on densification, mechanical, micro-structural and structure-properties relationship of magnesium aluminate spinel refractory aggregates prepared from Indian magnesite. Materials Characterization 99**,** 84-91.
Giordanengo, B., Benazzi, N., Vinckel, J., Gasser, J.G., Roubi, L., 1999. Thermal conductivity of liquid metals and metallic alloys. J. of Non-Crystalline Solids 250-252(1), 377-383.

Goldman, L.M., Kashalikar, U., Ramisetty, M., Jha, S., Sastri, S., 2017. Scale up of large ALON® and spinel windows., In: Proceedings of SPIE Window and Dome Technologies and Materials XV 10179, 101790J-14.
Graphite AM, Available online: https://www.graphite-am.co.uk/ (Accessed: 4/12/2022).
Greenstein, M., 1989. Optical-absorption aspects of laser soldering for high-density interconnects. Appl. Optics 28**,** 4595-4603.
Harris, D.C., 1998. Durable 3–5 μm transmitting infrared window materials. Infrared Physics & Technol. 39(4), 185-201.
Harris, D.C., Johnson, L.F., Seaver, R., Lewis, T., Turri, G., Bass, M., Zelmon, D.E., Haynes, N.D., 2013. Optical and thermal properties of spinel with revised (increased) absorption at 4 to 5 μm wavelengths and comparison with sapphire. Opt. Eng. 52**,** 087113-087113.
Heinzel, A., Hering, W., Konys, J., Marocco, L., Litfin, K., Muller, G., Pacio, J., Schroer, C., Stieglitz, R., Stoppel, L., Weisenburger, A., Wetzel, T., 2017. Liquid metals as efficient high-temperature heat-transport fluids. Energy Technol. 5**,** 1026-1036.
Hildebrand, J.H., 1918. The vapour pressure of liquid metals. J. American Chem. Soc. 40(1), 45–49.
Hinkley, J., Agrafiotis, C., Khalilpour, K. R., 2019. Solar thermal energy and its conversion to solar fuels via thermochemical processes, in: Khalilpour, K.R., Polygeneration with Polystorage for Chemical and Energy Hubs for Energy and Chemicals. Elsevier Inc., Oxford, pp. 247-286.
Ho, C.K., 2016. A review of high-temperature particle receivers for concentrating solar power. Appl. Therm. Eng. 109**,** 958-969.
Ho, C.K., Christian, J.M., Yellowhair, J.E., Armijo, K., Kolb, W.J., Jeter, S., Golob, M., Nguyen, C., 2019. On-Sun performance evaluation of alternative high-temperature falling particle receiver designs. J. Sol. Energy Eng. 141, 011009.
Ho, C.K., Iverson, B.D., 2014. Review of high-temperature central receiver designs for concentrating solar power. Renew. and Sustainable Energy Reviews 29**,** 835-846.
Hoffschmidt, B., Alexopoulos, S., Göttsche, J., Sauerborn, M., Kaufhold, O., 2012. High concentration solar collectors, in: Sayigh, A.A.M., Comprehensive Renewable Energy. Elsevier Inc., Boston, pp. 165-209.
Hou, Y., Chang, H., Song, K., Lu, C., Zhang, P., Wang, Y., Wang, Q., Rao, W., Liu, J., 2018. Coloration of liquid-metal soft robots: from silver-white to iridescent. ACS Appl. Materials & Interfaces 10(48), 41627– 41636.
Huang, Z.-S., Shen, C., Fan, L., Ye, X., Shi, X., Li, H., Zhang, Y., Lai, Y., Quan, Y.-Y., 2021. Experimental investigation of the anti-soiling performances of different wettability of transparent coatings: Superhydrophilic, hydrophilic, hydrophobic and superhydrophobic coatings. Sol. Energy Materials and Sol. Cells 225, 111053.
Ilse, K., Khan, M. Z., Voicu, N., Naumann, V., Hagendorf, C., Bagdahn, J., 2019. Advanced performance testing of anti-soiling coatings - Part II: Particle-size dependent analysis for physical understanding of dust removal processes and determination of adhesion forces. Sol. Energy Materials and Sol. Cells 202, 110049.
Imran Khan, M., Asfand, F., Al-Ghamdi, S.G., 2023. Progress in research and technological advancements of commercial concentrated solar thermal power plants. Sol. Energy 249, 183-226.
Incropera, F.P., DeWitt, D.P., Bergman, T.L., Lavine, A.S., 2017. Principles of heat and mass transfer, eighth ed. Wiley, New York.
Jack, J.R., Bowman, R.L., Spisz, E.W., Weigand, A.J., 1969. Solar absorptances and spectral reflectances of 12 metals for temperatures ranging from 300 to 500 K. NASA Technical Note D5353, Lewis Research Center, Washington D.C.
Karni, J., Kribus, A., Ostraich, B., Kochavi, E., 1998. A high-pressure window for volumetric solar receivers. J. Sol. Energy Eng. 120(2): 101–107.
Kehlhofer, R., Rukes, B., Hannemann, F., Stirnimann, F., 2009. Combined-cycle gas & steam turbine power plants, third ed. PennWell, Tulsa, Oklahoma.
Khvan, A.V., Babkina, T., Dinsdale, A.T., Uspenskaya, I.A., Fartushna, I.V., Druzhinina, A.I., Syzdykova, A.B., Belov, M.P., Abrikosov, I. A., 2019. Thermodynamic properties of tin: part I

experimental investigation, ab-initio modelling of α-, β-phase and a thermodynamic description for pure metal in solid and liquid state from 0 K. Calphad 65, 50-72.
Klosterman, D.A., Chartoff, R.P., Osborne, N.R., Graves, G.A., Lightman, A., Han, G., Bezeredi, A., Rodrigues, S., 1999. Development of a curved layer LOM process for monolithic ceramics and ceramic matrix composites. Rapid Prototyping J. 5(2), 61-71.
Kohl, S., Kaufmann, F., Schmidt, M., 2022. Why color matters—proposing a quantitative stability criterion for laser beam processing of metals based on their fundamental optical properties. Metals 12(7), 1118.
Kong, L.B., Huang, Y.Z., Que, W.X., Zhang, T.S., Li, S., Zhang, J., Dong, Z.L. Tang, D.Y., 2015. Transparent Ceramics. Cham: Springer Int. Publishing, Switzerland.
Kotzé, J.P., Von Backström, T.W., Erens, P.J., 2011. A combined latent thermal energy storage and steam generator concept using metallic phase change materials and metallic heat transfer fluids for concentrated solar power. In: 17th SolarPACES Conference. Granada, Spain.
Krishnamurti, R., 1973. Some further studies on the transition to turbulent convection. J. of Fluid Mechanics 60(2), 285-303.
Krishnan, S., Nordine P.C., 1993. In: Optical properties and emissivities of liquid metals and alloys. NASA Workshop on the Thermophysical Properties of Molten Materials, 19940020647.
Lakhdar, Y., Tuck, C., Binner, J., Terry, A., Goodridge, R., 2021. Additive manufacturing of advanced ceramic materials. Progress in Materials Sci. 116, 100736.
Lakshmipathy, B., Sivaraman, B., Senthilkumar, M., Kajavali, A. and Sivakumar, K., 2020. Technological improvement on energy-efficient methods applied to a solar cavity collector. Materials Sci. for Energy Technol. 3, 456-463.
Lauzier, N., 2004. View Factors. MATLAB Central File Exchange. Available in: https://www.mathworks.com/matlabcentral/fileexchange/5664-view-factors. (Accessed: 7/12/2022).
Le Roux, W.G., Bello-Ochende, T., Meyer, J.P., 2014. The efficiency of an open-cavity tubular solar receiver for a small-scale solar thermal Brayton cycle. Energy Conversion and Management 84, 457-470.
Leitner, M., Leitner, T., Schmon, A., Aziz, K., Pottlacher, G., 2017. Thermophysical Properties of Liquid Aluminum. Metallurgical and Materials Transactions A 48**,** 3036-3045.
Li, L., Coventry, J., Bader, R., Pye, J., Lipinski, W., 2016. Optics of solar central receiver systems: a review. Opt. Express 24**,** A985-A1007.
Li, L., Wang, B., Pottas, J., Lipiński, W., 2019. Design of a compound parabolic concentrator for a multi-source high-flux solar simulator. Sol. Energy 183, 805-811.
Li, X., Kong, W., Wang, Z., Chang, C., Bai, F., 2010. Thermal model and thermodynamic performance of molten salt cavity receiver. Renew. Energy 35, 981-988.
Liu, J., Wang, Z., Liu, H., Wang, X., Ma, Y., 2019. Effect of Y2O3 doping on the high-temperature properties of magnesia aluminate spinel refractories. J. of the Australian Ceramic Society 56, 1-6.
Liu, M., Lu, Y., Xie, Z.B. and Chow, G.M., 2011. Enhancing near-infrared solar cell response using upconverting transparent ceramics. Sol. Energy Materials and Sol. Cells 95(2), 800-803.
Lorenz, T., Klimm, E., Weiss, K.-A., 2014. Soiling and anti-soiling coatings on surfaces of solar thermal systems – featuring an economic feasibility analysis. Energy Procedia 48, 749-756.
Lorenzin, N., Abánades, A., 2016. A review on the application of liquid metals as heat transfer fluid in Concentrated Solar Power technologies. Int. J. of Hydrogen Energy 41**,** 6990-6995.
Lovegrove, K., Pye, J., 2012. Fundamental principles of concentrating solar power (CSP) systems, in: Lovegrove, K., Stein, W., Concentrating Solar Power Technology. Woodhead Publishing Ltd., pp. 16-67.
Maag, G., Falter, C. and Steinfeld, A., 2010. Temperature of a quartz/sapphire window in a solar cavity-receiver. J. Sol. Energy Eng. 133(1), 014501.
Mohammadi, M.M., Choi, S., Koirala, P., Jayatilaka, G.C., Ghousifam, N., Celio, H., Tehrani, M., 2022. Additive manufacturing of recyclable, highly conductive, and structurally robust graphite structures. Additive Manufacturing Letters 3, 100061.
Moran, K., Inumaru, J., Kawaji, M., 2002. Instantaneous hydrodynamics of a laminar wavy liquid film. Int. J. of Multiphase Flow 28(5), 731-755.

Morita, K., Maschek, W., Flad, M., Yamano, H. and Tobita, Y., 2006. Thermophysical properties of lead-bismuth eutectic alloy in reactor safety analyses. J. of Nuclear Sci. and Technol. 43(5), 526-536.
Muhich, C.L., Ehrhart, B.D., Al-Shankiti, I., Ward, B.J., Musgrave, C.B., Weimer, A.W., 2016. A review and perspective of efficient hydrogen generation via solar thermal water splitting. WIREs Energy Environ. 5, 261–287.
Maurya, A., Kumar, A., Sharma, D., 2022. A comprehensive review on performance assessment of solar cavity receiver with parabolic dish collector. Energy Sources, Part A: Recovery, Utilization, and Environmental Effects 44(2), 4808-4845.
Nath, A.K., 1988. Laser etching and dry processing. The Bulletin of Material Sci. 11, 159–166.
Nusselt, W., 1916. Die Oberflächenkondensation des Wasserdampfes. VDI-Zeitschriften, Frankfurt. vol. 60, pp. 541-546, 569-575.
Pacio, J., Singer, C., Wetzel, T., Uhlig, R., 2013. Thermodynamic evaluation of liquid metals as heat transfer fluids in concentrated solar power plants. Appl. Therm. Eng. 60(2)**,** 295-302.
Pacio, J., Wetzel, T., 2013. Assessment of liquid metal technology status and research paths for their use as efficient heat transfer fluids in solar central receiver systems. Sol. Energy 93**,** 11-22.
Phelan, P., Otanicar, T., Taylor, R., Tyagi, H., 2013. Trends and opportunities in direct-absorption solar thermal collectors. J. Therm. Sci. and Eng. Applications 5(2), 021003.
Pilkington, L.A.B., 1969. Review Lecture: The float glass process. In: Proceedings of the Royal Society of London. Series A: Mathematical and Physical Sci. 314(1516), 1-25.
Pitz-Paal, R., Botero, N.B., Steinfeld, A., 2011. Heliostat field layout optimization for high-temperature solar thermochemical processing. Sol. Energy 85(2), 334-343.
Qadri, S.N., Bayya, S.S., Villalobos, G., Kim, W., Hunt, M., Busse, L.E., Frantz, J.A., Shaw, L.B., Sanghera, J.S., Sadowski, B., Miklos, R., Aggarwal, I.D., Wilson, C.R., 2019. Spinel optics for high energy lasers. In: Proceedings of SPIE Window and Dome Techno. and Materials XVI 10985, 1098508-8.
Quan, Y.-Y., Zhang, L.-Z., 2017. Experimental investigation of the anti-dust effect of transparent hydrophobic coatings applied for solar cell covering glass. Sol. Energy Materials and Sol. Cells 160, 382-389.
Ramanathan, K.G., Yen, S.H., 1997. High-temperature emissivities of copper, aluminum, and silver. J. Opt. Soc. of America 67, 32-38.
Ries, H., Kribus, A., Karni, J., 1995. Nonisothermal receivers. J. Sol. Energy Eng. 117(3), 259–261.
Rinaldi, F., Binotti, M., Giostri, A., Manzolini, G., 2014. Comparison of linear and point focus collectors in solar power plants. Energy Procedia 49, 1491-1500.
Robinson, A., 2017. Ultra-high temperature thermal energy storage. part 1: concepts. J. of Energy Storage 13**,** 277-286.
Roldán Serrano, M.I., 2017. Concentrating solar thermal technologies: analysis and optimisation by CFD modelling. Cham: Springer Int. Publishing, Switzerland.
Romero, M., González-Aguilar, J., 2016. Next generation of liquid metal and other high-performance receiver designs for concentrating solar thermal (CST) central tower systems. Advances in Concentrating Sol. Therm. Research and Technol. 2017, 129-254.
Romero, M., González-Aguilar, J., 2014. Solar thermal CSP technology. Wiley Interdisciplinary Reviews: Energy and Environ. 3**,** 42-59.
Romero, M., Steinfeld, A., 2012. Concentrating solar thermal power and thermochemical fuels. Energy & Environ. Sci. 5(11). 9234-9245.
Röger, Marc, Rickers, C., Uhlig, R., Neumann, F. and Polenzky, C., 2009. Infrared-reflective coating on fused silica for a solar high-temperature receiver. J. Sol. Energy Eng. 131(2), 21004.
Röger, M., Pfänder, M. and Buck, R., 2006. Multiple air-jet window cooling for high-temperature pressurized volumetric receivers: testing, evaluation, and modeling. J. Sol. Energy Eng. 128(3), 265-274.
Sako, E.Y., Orsolini, H.D., Moreira, M., De Sousa Meneses, D., Pandolfelli, V.C., 2021. Emissivity of spinel and titanate structures aiming at the development of industrial high-temperature ceramic coatings. J. of the European Ceramic Society 41(4), 2958-2967.
Samanes, J., García-Barberena, J., Zaversky, F., 2015. Modeling solar cavity receivers: a review and comparison of natural convection heat loss correlations. Energy Procedia 69, 543-552.

Sandia, 1983. Sodium solar receiver experiment: final report. SAND82-8192. United States. Available online: https://www.osti.gov/biblio/5332177-sodium-solar-receiver-experiment-final-report (Accessed: 6/5/2022).

Sanghera, J., Bayya, S., Villalobos, G., Kim, W., Frantz, J., Shaw, B., Sadowski, B., Miklos, R., Baker, C., Hunt, M., Aggarwal, I., Kung, F., Reicher, D., Peplinski, S., Ogloza, A., Langston, P., Lamar, C., Varmette, P., Dubinskiy, M. ,Desandre, L., 2011. Transparent ceramics for high-energy laser systems. Opt. Materials 33(3)**,** 511-518.

Sanghera, J., Rock, B., Villalobos, G., Kim, W., Hunt, M., Sadowski, B., Bayya, S., Aggarwal, I., Imam, M.A., 2015. Highly transparent spinel windows by microwave sintering. In: Proceedings of SPIE Window and Dome Technol. and Materials XIV 9453, 945302-8.

Segal, A., 2012. Optimum layout of heliostat field when the tower-top receiver is provided with secondary concentrators. Report for SFERA, WP.13, Task 2, Weizmann Institute of Science, Israel.

Schiel, W.J.C., Geyer, M.A., 1988. Testing an external sodium receiver up to heat fluxes of 2.5 MW/m 2: Results and conclusions from the IEA-SSPS high flux experiment conducted at the central receiver system of the Plataforma Solar de Almeria (Spain), Sol. Energy 41**,** 255-265.

Schmitz, M., Schwarzbözl, P., Buck, R., Pitz-Paal, R., 2006. Assessment of the potential improvement due to multiple apertures in central receiver systems with secondary concentrators. Sol. Energy 80**,** 111-120.

Sharafat, S., Ghoniem, N., 2000. Summary of thermo-physical properties of Sn, and compounds of Sn-H, Sn-O, Sn-C, Sn-Li, and Sn-Si and comparison of properties of Sn, Sn-Li, Li, and Pb-Li. APEX Study CA 90095-1597. Mech. Aerospace Engr. Dept., University of California, Los Angeles.

Siegel, N., Gross, M., Ho, C., Phan, T., Yuan, J., 2014. Physical properties of solid particle thermal energy storage media for concentrating solar power applications. Energy Procedia 49, 1015-1023.

Singer, C., Buck, R., Pitz-Paal, R., Muller-Steinhagen, H., 2010. Assessment of solar power tower driven ultrasupercritical steam cycles applying tubular central receivers with varied heat transfer media. J. Sol. Energy Eng. Trans. 132, 041010.

Sobolev, V., 2010. Database of thermophysical properties of liquid metal coolants for GEN-IV: Sodium, lead, lead-bismuth eutectic (and bismuth). CK-CEN Belgian Nuclear Research Centre, Boeretang, Belgium. Avaliable online: https://inis.iaea.org/collection/NCLCollectionStore/_Public/43/095/43095088.pdf (Accessed: 6/6/2022).

Sova, R.M, Linevsky, M.J., Thomas, M.E., Mark, F.F., 1998. High-temperature infrared properties of sapphire, AlON, fused silica, yttria, and spinel. Infrared Physics & Technol. 39(4), 251-261.

Sepulveda, J.L., Loutfy, R.O., Ibrahim, S., Bilodeau, S. 2013. Large-size spinel windows and domes. In: Proceedings of SPIE Window and Dome Technologies and Materials XIII 8708, 870806-15.

Stein, W.H., Buck, R., 2017. Advanced power cycles for concentrated solar power. Sol. Energy 152**,** 91-105.

Steinfeld, A., Schubnell, M., 1993. Optimum aperture size and operating temperature of a solar cavity-receiver. Sol. Energy 50**,** 19-25.

Steinfeld, A., 2002. Solar hydrogen production via a two-step water-splitting thermochemical cycle based on Zn/ZnO redox reactions. Int. J. of Hydrogen Energy 27**,** 611-619.

Steinfeld, A., Palumbo, R., 2001. Solar thermochemical process technology. Encyclopedia of Physical Sci. and Technol. 15, 237–256.

Tammen, Bobby, J., 1984. Liquid metal solar power system. U.S. Patent and Trademark Office, US4454865A.

Tan, T., Chen, Y., Chen, Z., Siegel, N. and Kolb, G.J., 2009. Wind effect on the performance of solid particle solar receivers with and without the protection of an aerowindow. Sol. Energy 83(10), 1815-1827.

Thorn R.J., Simpson O.C., 1953. Spectral emissivities of graphite and carbon. J. of Appl. Physics 24(5), 633-639.

Tseluiko, D., Blyth, M.G., Papageorgiou, D.T., 2013. Stability of film flow over inclined topography based on a long-wave nonlinear model. J. of Fluid Mechanics 729, 638-671.
Tsuji, T., Nagano, Y., 1988. Characteristics of a turbulent natural convection boundary layer along a vertical flat plate. Int. J. of Heat and Mass Transfer 31**,** 1723-1734.
Ujihara, K., 1972. Reflectivity of Metals at High Temperatures. J. of Appl. Physics 43**,** 2376-2383.
Unifrax, 2018. Excelfrax® microporous insulation: product information sheet. New York, U.S. Available online: https://www.unifrax.com/wp-content/uploads/2018/08/Form-C-1500-Excelfrax-Microporous-Insulation-2-03.pdf (Accessed: 6/6/2022).
Vant-Hull, L.L., 2021. Central tower concentrating solar power systems, in: Lovegrove, K. and Stein, W. (2) Concentrating Solar Power Technology Energy. Woodhead Publishing, pp. 267-310.
Velusamy, K., Sundararajan, T., Seetharamu, K.N., 2001. Interaction effects between surface radiation and turbulent natural convection in square and rectangular enclosures. ASME. J. Heat Transfer 123(6), 1062–1070.
Villalobos, G., Bayya, S., Kim, W., Sanghera, J., Sadowski, B., Miklos, R., Florea, C. and Aggarwal, I., 2012. Polished spinel directly from the hot press. Advances in Ceramic Armor VIII, 105-109.
Wang, F., Cheng, L., Mei, H., Zhang, Q., Zhang, L., 2014. Effect of Surface Microstructures on the Infrared Emissivity of Graphite. Int. J. of Thermophysics 35**,** 62-75.
Wang, W., Ye, F., Mu, W., Dutta, J. and Laumert, B., 2021. A new high-temperature durable absorber material solution through a spinel-type high solar absorptivity coating on Ti2AlC MAX phase material. ACS Appl. Materials & Interfaces 13(37), 45008-45017.
Wu, W., Amsbeck, L., Buck, R., Uhlig, R., Ritz-Paal, R., 2014. Proof of concept test of a centrifugal particle receiver. Energy Procedia 49**,** 560-568.
Yih, C.S., 1963. Stability of liquid flow down an inclined plane. The Physics of Fluids 6(3), 321-334.
Zhang, J., Wang, W., Zhou, S., Yang, H., Chen, C., 2019. Transparent dust removal coatings for solar cell on mars and its anti-dust mechanism. Progress in Organic Coatings 134, 312-322.
Zhang, Y., Cai, Y., Hwang, S., Wilk, G., DeAngelis, F., Henry, A., Sandhage, K.H., 2018. Containment materials for liquid tin at 1350 °C as a heat transfer fluid for high temperature concentrated solar power. Sol. Energy 164**,** 47-57.
Zheng, Z.-J., Xu, Y., 2018. A novel system for high-purity hydrogen production based on solar thermal cracking of methane and liquid-metal technology: thermodynamic analysis. Energy Conversion and Management 157, 562-574.
Zou, C., Zhang, Y., Falcoz, Q., Neveu, P., Zhang, C., Shu, W., Huang, S., 2017. Design and optimization of a high-temperature cavity receiver for a solar energy cascade utilization system. Renew. Energy 103, 478-489.